CM² MAGAZINE

第 37 期

南方科技大学海洋磁学中心主编

创刊词

海洋是生命的摇篮，是文明的纽带。地球上最早的生命诞生于海洋，海洋里的生命最终进化成了人类，人类的文化融合又通过海洋得以实现。人因海而兴。

人类对海洋的探索从未停止。从远古时代美丽的神话传说，到麦哲伦的全球航行，再到现代对大洋的科学钻探计划，海洋逐渐从人类敬畏崇拜幻想的精神寄托演变成可以开发利用与科学研究的客观存在。其中，上个世纪与太空探索同步发展的大洋科学钻探计划将人类对海洋的认知推向了崭新的纬度：深海（deep sea）与深时（deep time）。大洋钻探计划让人类知道，奔流不息的大海之下，埋藏的却是亿万年的地球历史。它们记录了地球板块的运动，从而使板块构造学说得到证实；它们记录了地球环境的演变，从而让古海洋学方兴未艾。

在探索海洋的悠久历史中，从大航海时代的导航，到大洋钻探计划中不可或缺的磁性地层学，磁学发挥了不可替代的作用。这不是偶然，因为从微观到宏观，磁性是最基本的物理属性之一，可以说，万物皆有磁性。基于课题组的学科背景和对海洋的理解，我们对海洋的探索以磁学为主要手段，海洋磁学中心因此而生。

海洋磁学中心，简称 CM^2，一为其全名“Centre for Marine Magnetism”的缩写，另者恰与爱因斯坦著名的质能方程 $E = MC^2$ 对称，借以表达我们对科学巨匠的敬仰和对科学的不懈追求。

然而科学从来不是单打独斗的产物。我们以磁学为研究海洋的主攻利器，但绝不仅限于磁学。凡与磁学相关的领域均是我们关注的重点。为了跟踪反映国内外地球科学特别是与磁学有关的地球科学领域的最新研究进展，海洋磁学中心特地主办 CM^2 Magazine，以期与各位地球科学工作者相互交流学习、合作共进！

“海洋孕育了生命，联通了世界，促进了发展”。 21 世纪是海洋科学的时代，由陆向海，让我们携手迈进中国海洋科学的黄金时代

目 录

岩石磁学演绎 1

第 27 章　赤铁矿 1

海磁快讯 **5**

海洋磁学中心欢送陈艇博士、迎接张亚南科研助理 5

文献导读 **6**

1. 氧同位素 19 和 20 期地中海西部海洋和陆地的气候变化 6
2. 古新世-始新世极热期间单一物种腰鞭毛虫包囊碳同位素生态学 10
3. 美国加州北部三个同时喷发的中更新世拉斑玄武岩：观察一个正在拉张的弧后盆地下的地壳岩浆迁移 13
4. 深海沉积物中逆磁化率结构:对磁小体丰度和排列的影响 16
5. 48-40 ka 放射性碳时间尺度的扩展膨胀以及尼安德特人和智人的重叠时间 18
6. 南海西南次海盆构造主导的海底扩张---来自地震学的证据 20
7. 地中海地幔动力学的地形表现 23
8. 中国中部过去千年的水汽变化及其与热带太平洋和北大西洋的联系 25
9. 全球风尘循环和大洋铁输入 30
10. 中国中部新石器时代晚期的高可信度的古强度结果 32
11. 晚更新世中亚伊犁盆地火迹与古气候变化和人类活动之间的潜在联系 34
12. 气泡对玄武岩熔岩流流变学的影响:大规模两相实验的启示 36
13. 末次冰期气候突变事件的时间同步性 38

岩石磁学演绎

第 27 章　赤铁矿

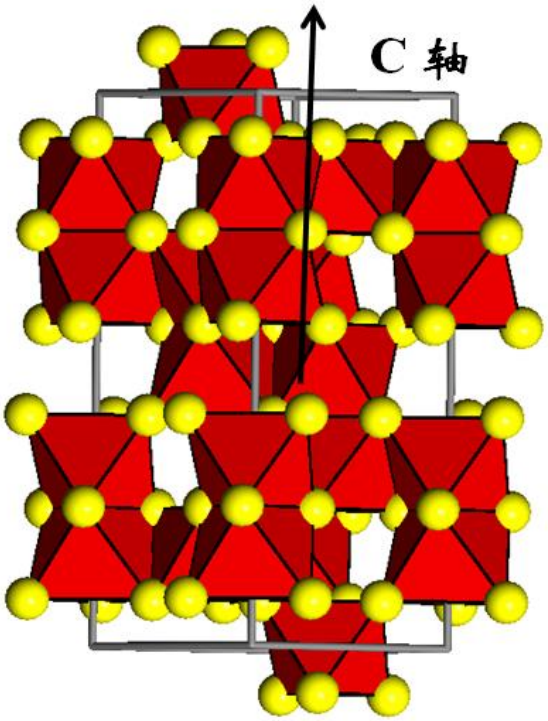

图 1　赤铁矿的晶格结构。

赤铁矿（Fe_2O_3）具有刚玉结构，一个 FeO_6 组合为一个八面体。相邻两层 Fe^{3+} 的磁矩排列方向刚好相反，相互抵消，因此赤铁矿具有反铁磁性（Antiferromagnetism）。每一层铁离子组成的面叫做 C 面，垂直于 C 面叫做 C 轴。

赤铁矿的 T_C 比磁铁矿要高，大约为 670°。其晶胞参数

a = b = 0.5034 nm

c = 1.3752 nm

赤铁矿 M_s 很小（~0.4 Am^2/kg），比磁铁矿小两个数量级。因此，其形状各向异性能就很小，磁结晶各向异性能提供主要的磁能。磁结晶各向异性能与 M_s 呈反比，也就是说 M_S 越小，其矫顽力就越大。磁铁矿的矫顽力一般在 20 mT 上下，而赤铁矿的矫顽力可以高达几百 mT，甚至更高。这就给了我们一个契机，可以利用磁铁矿和赤铁矿矫顽力的巨大差别，来确定二者对一块样品磁性的贡献。

首先，给一块样品在 X 轴方向加一个饱和场（比如 1 T），磁铁矿和赤铁矿都会饱和，样品的剩磁为 IRM_{1T}。然后在反方向加一个 300 mT 的场，让样品重新磁化。所有剩磁矫顽力小于 300 mT 的颗粒，其磁矩都会沿着反方向被饱和磁化，而剩磁矫顽力大于 300 mT 的颗粒，其磁矩仍然保持正向磁化。此时，样品中就含有两种相反的磁矩，整体剩磁叫 IRM_{-300mT}。

如果想要估算高矫顽力成分（Hard IRM, HIRM）的贡献，我们可以把两个剩磁相加：

$HIRM = 0.5 *（IRM_{1T} + IRM_{-0.3T}）$

其中的系数 0.5 是因为，高矫顽力组分对 IRM_{1T} 和 $IRM_{-0.3T}$ 都有贡献。相加时，软磁组分被抵消，而硬磁组分被重复计算，所以需要除以二。另外，在计算 HIRM 时，一定要注意，IRM_{1T} 和 $IRM_{-0.3T}$ 都是矢量，而超导仪器测出的剩磁强度那项只显示数值，不显示方向，所以在进行二者相加时，一定要注意 $IRM_{-0.3T}$ 倾角方向，不能简单的进行数值相加，否则就会引起错误的解释。

一般情况下，HIRM 越高，表示样品中的高矫顽力组分的含量越高。

除了计算 HIRM，还可以利用上面的参数计算高矫顽力和低矫顽力成分之间的相对含量：

$S = -IRM_{-0.3T} / IRM_{1T}$

这个比值越接近于 1，表示软磁组分含量高，S 比值越低，表示硬磁组分含量高。

上面我们选择 300 mT 作为阀门值，其实还可以选择其它的阀门值，比如 100 mT。为了区分期间，我们重新定义:

$HIRM_{x\ mT} = 0.5 * (IRM_{1T} + IRM_{x\ mT})$

后来的研究表明，赤铁矿的剩磁矫顽力变化很大，尤其是含铝赤铁矿，很多 Al-Hm 的剩磁矫顽力就小于 300 mT，于是传统的 $HIRM_{-300mT}$ 就不能真正代表赤铁矿的含量变化。

为了解决这一难题，Liu et al. (2007)提出 L 比值的概念：

$L = HIRM_{-300mT} / HIRM_{-100\ mT}$

L 比值与高矫顽力分的剩磁矫顽力正相关。L 比值越大，表示其剩磁矫顽力越大。只有当 L 比值变化不大时，剩磁矫顽力的变化对 HIRM 影响较小，HIRM

才能被用来衡量高矫顽力组分的变化。如果 L 比值变化很大，说明 HIRM 不再单纯地表示高矫顽力组分的含量。反而 L 比值本身可能代表着高矫顽力组分物源的变化。

和磁铁矿相似，赤铁矿也有一个低温转换温度，发生在 250 K 左右，叫做 Morin 转换，该温度叫做 T_M。表现在剩磁方面，就是剩磁会突然发生变化。

我们来一起做一个实验。找一个晶型完美的赤铁矿，首先我们在 300 K 沿着 C 面方向加场，让赤铁矿获得一个剩磁。然后在 C 面和 C 轴方向，同时测量剩磁随着温度降低的变化特征。在 250 K 左右，我们发现沿着 C 面的剩磁突然大幅度下降，而沿着 C 轴方向上的剩磁突然大增。这说明在 300 K 沿着 C 面获得的剩磁在 T_M 突然转向到了 C 轴。所有这种磁矩突然转向的行为都可以用能量最小原理来解释。

我们来考察一个正向放置的碗，此时碗底是能量最小状态。而对于一个反向放置的碗，其碗底则是一个能量最大状态。计算磁能需要一个系数，这个系数是随着温度变化的。当这个系数在 T_M 变符号时，能量最小状态就发生改变。在 TM 之上，M 沿着 C 面定向排列，而在 T_M 之下，M 会发生 90°偏转，变成沿着 C 轴定向排列。

T_M 也不是一个固定的值，和 T_V 一样，和赤铁矿的晶型、所含杂质都有关系。自然界中赤铁矿大部分以纳米颗粒存在，很难用 T_M 来检测其存在。如果样品真的显示了 T_M，这就说明其所含赤铁矿颗粒的粒径偏大，也比较纯。

在 T_M 之下，我们发现，赤铁矿的剩磁并不为零，这是什么原因？

这种情况下，赤铁矿的剩磁主要来源于缺陷剩磁，也就是说赤铁矿在晶体内含有一定的晶格缺陷，正反两个方向磁矩不再匹配，于是产生了剩磁。

可是，当温度逐渐回升，在跨越 T_M 之后，又恢复了一部分剩磁，这又是怎么一回事？

在赤铁矿晶体内部存在着不少的晶格缺陷，在这些部位，当温度回升时，会重新长出磁畴，剩磁会增长，但是肯定恢复不到原来的状态。

Özdemir and Dunlop (2006)证实了这一点。T_M 之下的剩磁和经过 LTC 之后的室温剩磁具有很好的正相关性。这说明 LTC 之后的室温剩磁确实受到晶格缺陷控制。

赤铁矿的晶体一般呈板状，在不同的环境下形成的赤铁矿形状差异较大。这种板状晶型很容易产生 DRM 倾角浅化问题。纳米级赤铁矿显示红色，是极好的染色材料。我们看到土壤红通通的，是因为含有很多成土作用产生的纳米赤铁矿。火星表面是红通通的，也是因为其表层土壤里含有大量的纳米赤铁矿。所以，研究赤铁矿不仅对地球有意义，对探索火星也会帮助很大。

赤铁矿除了对环境敏感，其参数可作为环境变化指标，它本身还是古地磁学中天然剩磁的重要载体。磁铁矿的 SD 粒径区间很狭窄，在几十到一百纳米之间。而赤铁矿 SD 的下边界和磁铁矿类似，几十个纳米，其上边界可达十几个微米。也就是说自然界中存在的赤铁矿几乎全在 SD 区间。

纳米级赤铁矿大多和沉积化学风化有关，是后期形成的，容易携带 CRM。而粗颗粒的赤铁矿是源区物理风化产生，在沉积区携带的是 DRM。判断样品中赤铁矿携带剩磁的机制，一直是古地磁学的前沿科学问题。

姜兆霞博士通过合成一系列的含铝赤铁矿，在实验室进行 DRM 沉积实验和 CRM 获得实验，发现 CRM 和 DRM 的热解阻谱完全不一样。携带 CRM 的赤铁矿小，T_B 值相对低，很容易被热退磁，其退磁谱相对宽泛。而携带 DRM 的赤铁矿颗粒相对较大，其解阻温度相对要高，不容易在低温解阻。这种解阻谱的显著区别成为目前判别赤铁矿 CRM 和 DRM 机制的重要方法之一。

赤铁矿与其他矿物不同，MD 颗粒比 SD 颗粒更容易获得 TRM。MD 赤铁矿的 TRM 很高，只比 SD 磁铁矿低一个数量级，这为我们以后的研究提供了一个新的思路，要重视 MD 赤铁矿的贡献（Kletetschka et al., 2000）。

海磁快讯

海洋磁学中心欢送陈艇博士、迎接张亚南科研助理

为祝贺南方科技大学海洋磁学中心陈艇研究助理教授前往重庆师范大学任教和欢迎张亚南科研助理入职，海洋磁学中心在 2020 年 9 月 2 日晚上组织了聚餐活动。各位老师和同学纷纷送上祝福，祝福陈老师在新的岗位上工作顺利，取得更多成果。

陈艇博士于 2017 年入职南科大，历任助理研究员、研究助理教授。在南科大工作期间，获得国家自然科学基金委青年项目资助，主要进行“上新世亚北极太平洋硅藻种群特征及其环境控制因素”的研究。陈艇博士在岩石磁学和硅藻鉴定方面有很深的专业功底，极大地促进了课题组的交叉研究。

本次活动同时欢迎张亚南科研助理加入海洋磁学中心，为海洋磁学中心注入了新鲜血液。张亚南硕士毕业于中科院南海所，期待他在海洋磁学中心取得更大的进步！

文献导读

1. 氧同位素 19 和 20 期地中海西部海洋和陆地的气候变化

翻译人：仲义 zhongy@sustech.edu.cn

Francesco Toti, Adele Bertini, Angela Girone et al., Marine and terrestrial climate variability in the western Mediterranean Sea during marine isotope stages 20 and 19 [J]. Quaternary Science Reviews, 2020, 243, 106486.
https://doi.org/10.1016/j.quascirev.2020.106486.

摘要：氧同位素 20 和 19 期的气候变化往往通过环爱琴海（西地中海地区）的海洋和陆地气候记录。利用 ODP 976 沉积物样品获得高时间分辨率（平均分辨率为 450 年）孢粉学（花粉和孢子）和钙质浮游生物（颗石藻和有孔虫）记录。这些结果并结合最新的 δ18OG.bulloides 指标建立的完整的年代学框架，可以进一步讨论古环境变化。较冷的阶段，包括 MIS 20 晚期和 MIS19b-a 期间的几次寒冷期，在陆地记录中表现为草原和半沙漠类为主的开阔植被的扩张。同时，在地中海西部表现为北大西洋极地浮游有孔虫类的入侵特征。在 MIS 19c 和 MIS 19b-a 的间期表现为温带森林类的扩张，这与同时期暖水种钙质浮游生物群的扩张一致。陆地和海洋记录中都表现为岁差和千年-亚千年尺度上的气候变化，突出了地中海西部地区对轨道强迫和北半球高纬度地区气候系统的快速振荡的响应。中-西地中海和北大西洋气候动态包括区域性和全球气候过程时间空间上的梯度变化，有助于重建早-中更新世过渡时期地球气候动力学和海洋对陆地的响应。这些新的证据也提高了我们对于 MIS 19c 的认识，因为它的轨道几何学特征，被认为是与全新世最接近的。

ABSTRACT: The climate variability within late Marine Isotope Stage (MIS) 20 and MIS 19 is examined with particular reference to the response of marine and terrestrial realms in the area surrounding the Alboran Sea (western Mediterranean Sea). Sediment samples from the Ocean Drilling Program Site 976 were used to derive high temporal resolution (average resolution of 450 years) palynological (pollen and spores) and calcareous plankton (coccolithophores and

foraminifera) records. These data, together with the new δ18OG.bulloides, make it possible to discuss the paleoenvironmental changes within a well constrained chronological frame. Cooler phases, including late MIS 20 and several cold spells during MIS 19b-a, are marked, on land, by the expansion of open vegetation formations dominated by steppe and semi-desert taxa. At the same time, the western Mediterranean Sea is marked by the incursion of North Atlantic polar-water planktonic taxa. MIS 19c and interstadials of MIS 19b-a are characterized by the spread of prevalent temperate forest taxa that parallel the expansion of warm-water calcareous plankton taxa during periods of lighter $\delta^{18}O$. Climate variations at both precessional and millennial to sub-millennial time-scales, expressed by on land and marine signals, highlight the sensitivity of the western Mediterranean area to both orbital forcing and rapid internal oscillations of the climate systems involving remote connections with North Hemisphere high latitudes. The correlation within the central-western Mediterranean and North Atlantic climate dynamics including the time/spatial gradients related to regional and global climate processes contributes to the reconstruction of the Earth climate dynamics and marine vs land responses, in full Early-Middle Pleistocene transition. These new evidences also provide an opportunity to improve knowledge of MIS 19c now considered, due to its orbital geometry, the best orbital analogue to the Holocene.

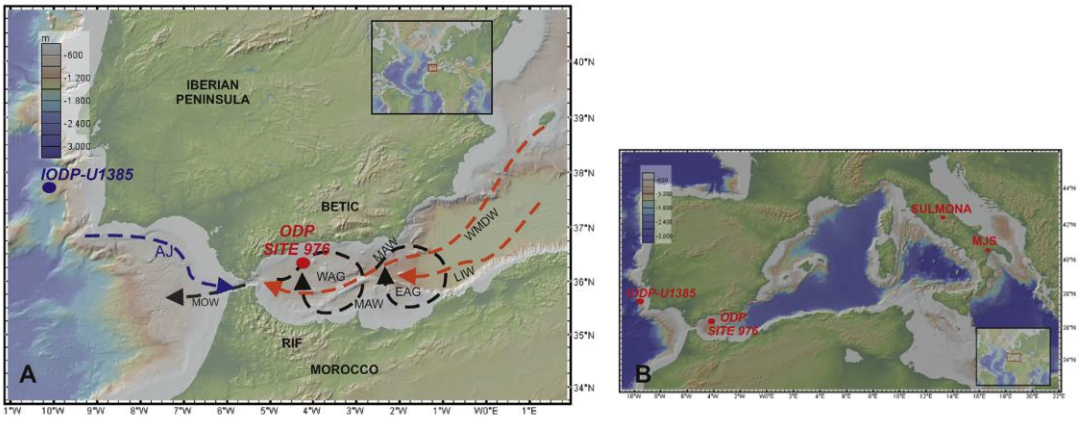

Figure 1. A) Location of ODP Site 976 in the Alboran Sea (western Mediterranean), bathymetry of the area and modern-day oceanographic circulation: AJ (Atlantic Jet), MOW (Mediterranean Outflow Water), WMDW (Western Mediterranean Deep Water), LIW (Levantine Intermediate Water), MAW (Modified Atlantic Water), WAG (Western Alboran Gyre), EAG (Eastern Alboran Gyre). B) Location

of IODP U1385, Sulmona and Montalbano Jonico (MJS) sites.

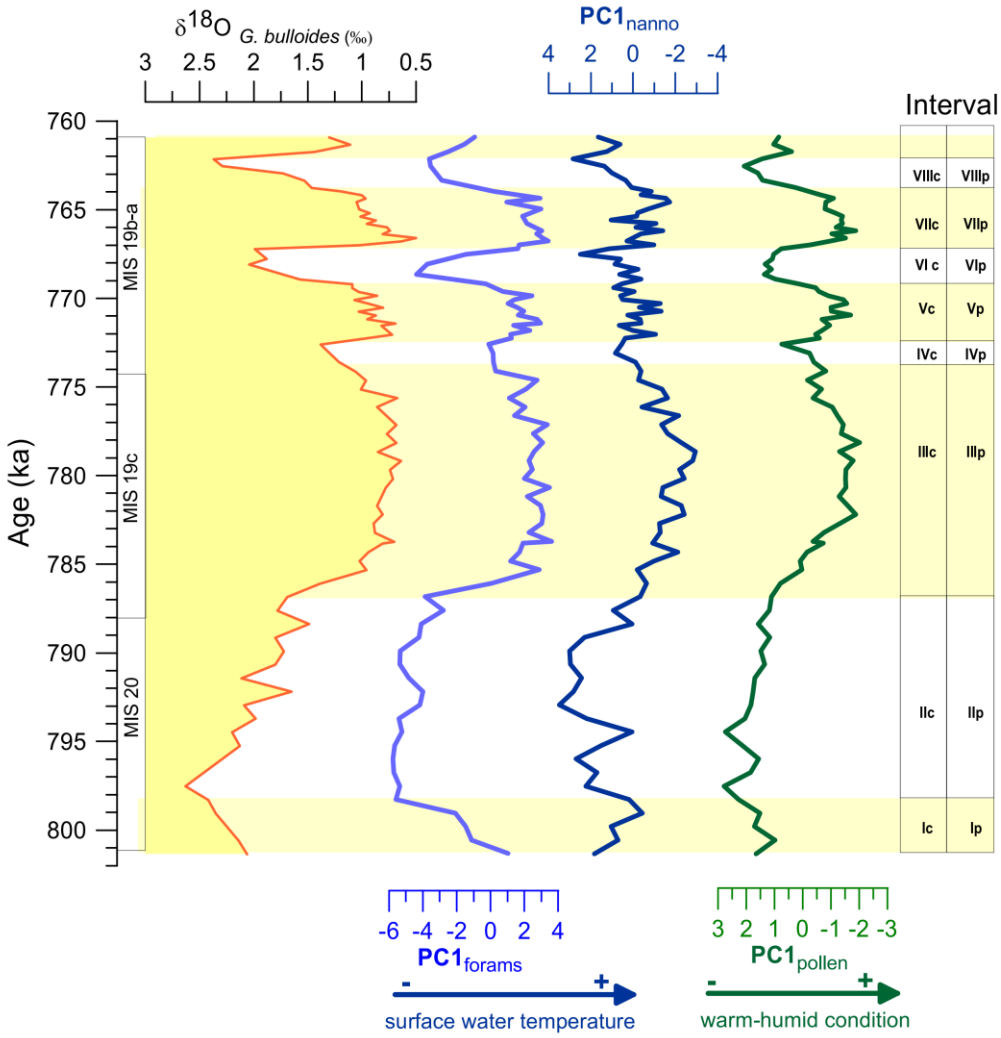

Figure 2. First components obtained by Principal Component Analysis (PCA) performed on assemblages of planktonic foraminifera, coccolithophores and pollen at the study site, plotted against the d18O vs time. On the right the intervals discriminated by the PCA on calcareous plankton (I-VIIIc) and pollen (I-VIIIp) assemblages.

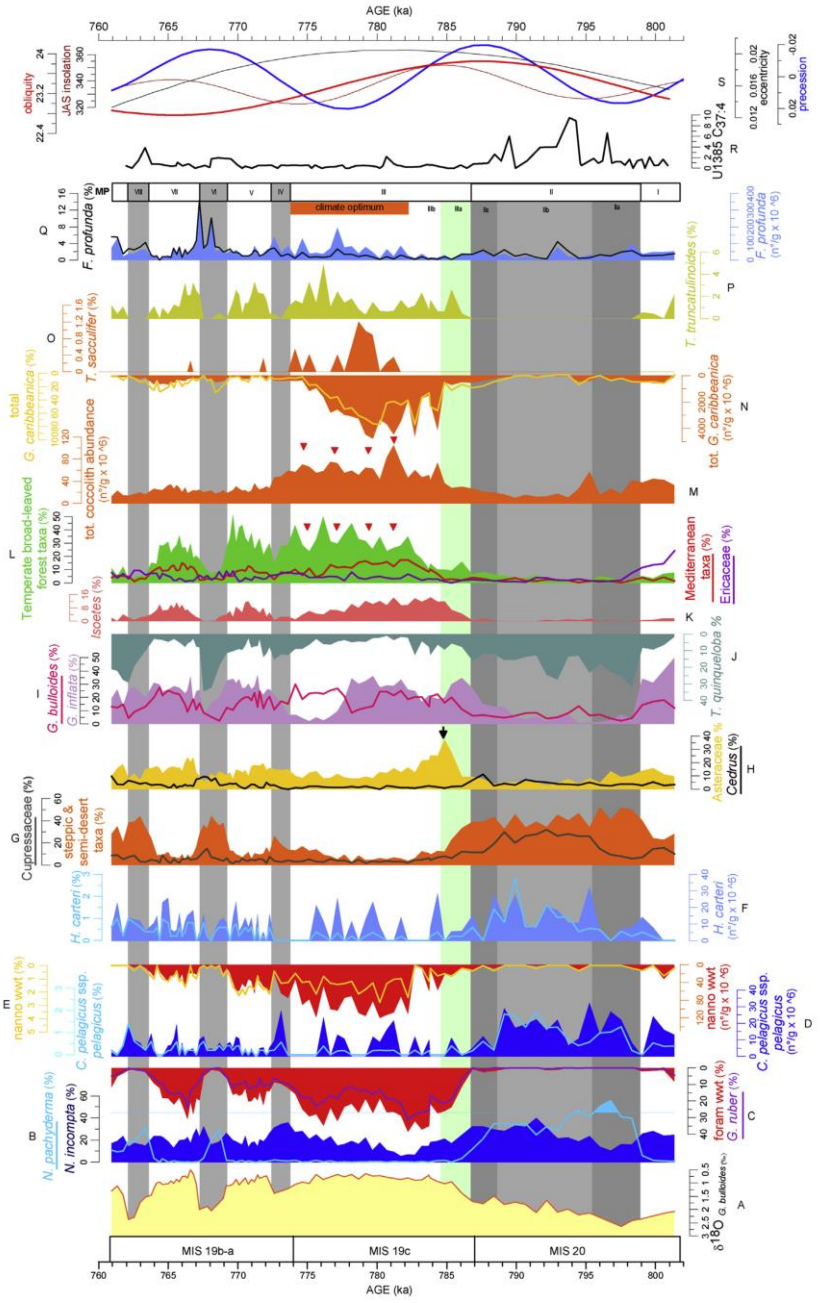

Figure 3. Abundance patterns of calcareous plankton and pollen key taxa (BeQ) plotted against d18O (A) vs time at the ODP Site 976. On the right the Merged Phases (MP I-VIII) according to biotic proxies at the study site, and C37:4 at the IODP Site U1385 (Rodriguez et al., 2017). Obliquity, precession and insolation patterns are shown according to Laskar et al. (2004). Red arrows indicate temperate forest contractions and increase of total coccolithophore abundances. Black arrow indicates event 1 (Bertini et al., 2015). (For interpretation of the references to colour in this figure legend, the reader is referred to the Web version of this article.)

2. 古新世-始新世极热期间单一物种腰鞭毛虫包囊碳同位素生态学

翻译人：蒋晓东 jiangxd@sustech.edu.cn

Sluijs A, van Roij L, Frieling J., Single-species dinoflagellate cyst carbon isotope ecology across the Paleocene-Eocene Thermal Maximum [J]. Geology, 2018, 46, 79–82
https://doi.org/10.1130/G39598.1

摘要：本研究从古新世-始新世极热期（PETM）沉积物中挑选出特定种属的腰鞭毛虫化石包囊，该样品来自美国新泽西州巴士河剖面。利用全新的激光剥蚀-同位素质谱对该化石进行了稳定碳同位素（$\delta^{13}C$）。该结果与碳酸盐 $\delta^{13}C$ 记录一致，即均呈现出显著的负漂移，这意味着腰鞭毛虫包囊 $\delta^{13}C$ 主要受控于溶解态无机碳。种属间显著的持续的 $\delta^{13}C$ 差别反应了栖息环境和生命循环过程以及对 pCO_2 不同的响应。在 PETM 期间种属间降低的种群和丰度变化，表明是时间或空间受限制的生态环境。本研究基于有机微化石分析为生态和演化的重建提供了一个新的方法。

ABSTRACT: We present the first ever species-specific fossil dinoflagellate cyst stable carbon isotope ($\delta^{13}C$) records, from the Bass River Paleocene- Eocene Thermal Maximum (PETM) section in New Jersey (USA), established using a novel coupled laser ablation– isotope ratio mass spectrometer setup. Correspondence with carbonate δ13C records across the characteristic negative carbon isotope excursion indicates that the δ13C of dissolved inorganic carbon exerts a major control on dinocyst δ13C. Pronounced and consistent differences between species, however, reflect different habitats or life cycle processes and different response to pCO_2. Decreased interspecimen variability during the PETM in a species that also drops in abundance suggests a more limited niche, either in time (seasonal) or space. This opens a new approach for ecological and evolutionary reconstructions based on organic microfossils.

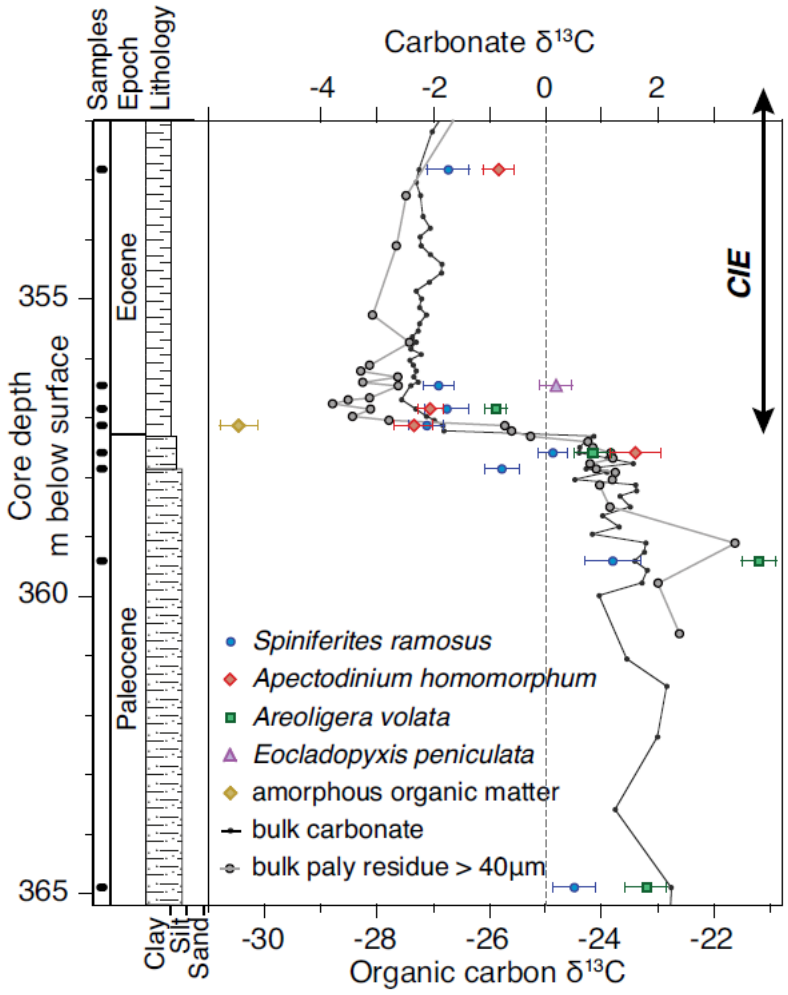

Figure 1. Dinocyst species-specific carbon isotope records from the Paleocene-Eocene Thermal Maximum (PETM) at Ocean Drilling Program Site Bass River, New Jersey, USA. The bulk carbonate record is from John et al. (2008), and the bulk palynological (paly) >40 µm record that dominantly comprises dinocysts is from Sluijs et al. (2007). Data points are mean values of 20–50 analyses on single specimens of Apectodinium homomorphum and Areoligera volata and 3–5 specimens of Spiniferites ramosus and *Eocladopyxis peniculata*. Error bars reflect 1 standard error of the mean. The $\delta^{13}C$ scales are offset by 25‰. Values are expressed (‰) relative to the Vienna Peedee belemnite standard. CIE—carbon isotope excursion.

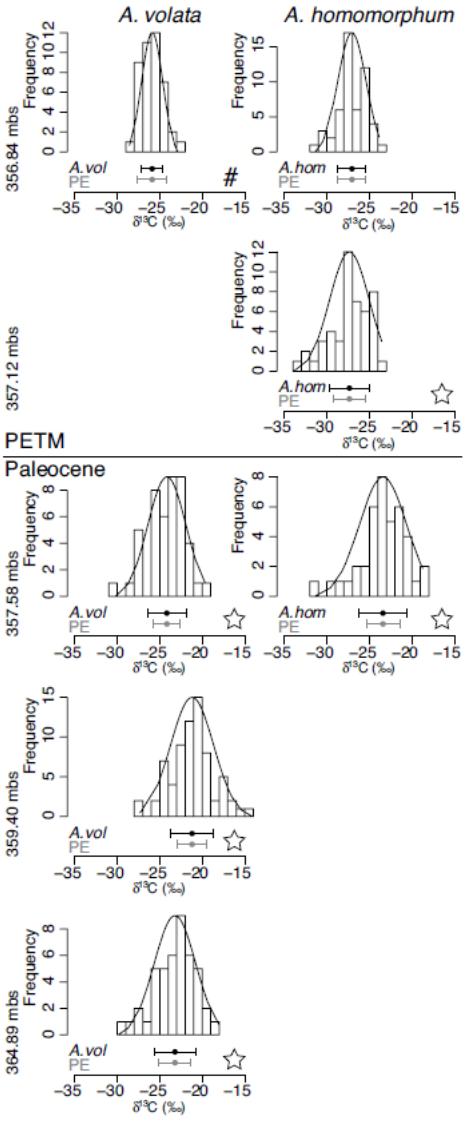

Figure 2. Frequency distribution of $\delta^{13}C$ analyses of individual Areoligera volata and Apectodinium homomorphum specimens (mbs—m below surface). Error bars reflect 1 standard error of the mean of dinocyst $\delta^{13}C$ analyses and the International Atomic Energy Agency CH-7 polyethylene (PE) standard. The variance of A. volata in the sample marked by # is significantly smaller than that of the PE standard, while stars indicate samples in which dinocyst $\delta^{13}C$ variance significantly exceeds that of the standard ($p < 0.05$).

3. 美国加州北部三个同时喷发的中更新世拉斑玄武岩：观察一个正在拉张的弧后盆地下的地壳岩浆迁移

翻译人：冯婉仪 fengwy@sustech.edu.cn

Downs D T, Champion D E, Muffler P, et al. Simultaneous Middle Pleistocene eruption of three widespread tholeiitic basalts in northern California (USA): Insights into crustal magma transport in an actively extending back arc[J]. Geology, 2020, 48.

https://doi.org/10.1130/G48076.1

摘要：绘图和年代学对于理解不同构造背景下的火山时空变化趋势至关重要。在美国加州北部的 Cascades 弧后盆地发育大量熔岩流和正断层，但传统的绘图方法难以区分年龄超过 200 ka 的拉斑玄武岩。古地磁和化学为 Tennant、Dry Lake 以及 Hammond Crossing 玄武岩的对比提供了独立的方法。这些化学性质相似的玄武岩的古地磁分析结果具有显著的重叠，而统计分析显示只有百万分之七的概率它们相似的平均剩磁方向是随机产生的。这些玄武岩的 $^{40}Ar/^{39}Ar$ 年龄也有重叠，分别为 272.5±30.6 ka（Tennant)、305.8±23.9 ka（Dry Lake）以及 300.4±15.2 和 322.6±17.4 ka（Hammond Crossing）。化学和古地磁分析表明，这些空间分布的玄武岩是同时（不确定度小于 100 年）喷发的，因此我们利用 305.5±9.8 ka（加权平均值）作为它们的喷发年龄。它们的喷发口在 39km 的范围内沿 N25°W 方向排列。Tennant 地区的岩浆喷发量最大（3.55 ± 0.75 km^3），并且处于最高的海拔，而其东南偏南方向的 Dry Lake（0.75 ± 0.15 km^3）和 Hammond Crossing（0.15 ± 0.05 km^3）的岩浆喷发量和海拔均逐渐降低。我们认为发育最演化、最富 SiO_2 的岩浆的 Tennant 喷发口之下的岩浆垂直向上运移，并在脆性地壳中伴随侧向岩脉传播。岩脉沿着北北西向的正断层传播，大致正交于东-西向的弧后扩张（0.3–0.6 mm/yr）方向。

ABSTRACT: Mapping and chronology are central to understanding spatiotemporal volcanic trends in diverse tectonic settings. The Cascades back arc in northern California (USA) hosts abundant lava flows and normal faults, but tholeiitic basalts older than 200 ka are difficult to discriminate by classic mapping methods. Paleomagnetism and chemistry offer independent

means of correlating basalts, including the Tennant, Dry Lake, and Hammond Crossing basalt fields. Paleomagnetic analysis of these chemically similar basalts yield notable overlap, with statistical analysis yielding 7 chances in 1,000,000 that their similar mean remanent directions are random. These basalts also have overlapping $^{40}Ar/^{39}Ar$ ages of 272.5 ± 30.6 ka (Tennant), 305.8 ± 23.9 ka (Dry Lake), and 300.4 ± 15.2 and 322.6 ± 17.4 ka (Hammond Crossing). Chemical and paleomagnetic analyses indicate that these spatially distributed basalts represent simultaneous (<100 yr uncertainty) eruptions, and thus we use 305.5 ± 9.8 ka (weighted mean) as the eruption age. Their vents align on a N25°W trend over a distance of 39 km. Tennant erupted the largest volume (3.55 ± 0.75 km^3) at the highest elevation; both factors decay to the south-southeast at Dry Lake (0.75 ± 0.15 km^3) and Hammond Crossing (0.15 ± 0.05 km^3). We propose vertical magma ascent beneath the Tennant vent area, where the most evolved, high-SiO_2 magma erupted, with lateral dike propagation in the brittle crust. Propagation was near orthogonal to east-west extension (0.3–0.6 mm/yr) along northnorthwest–trending normal faults.

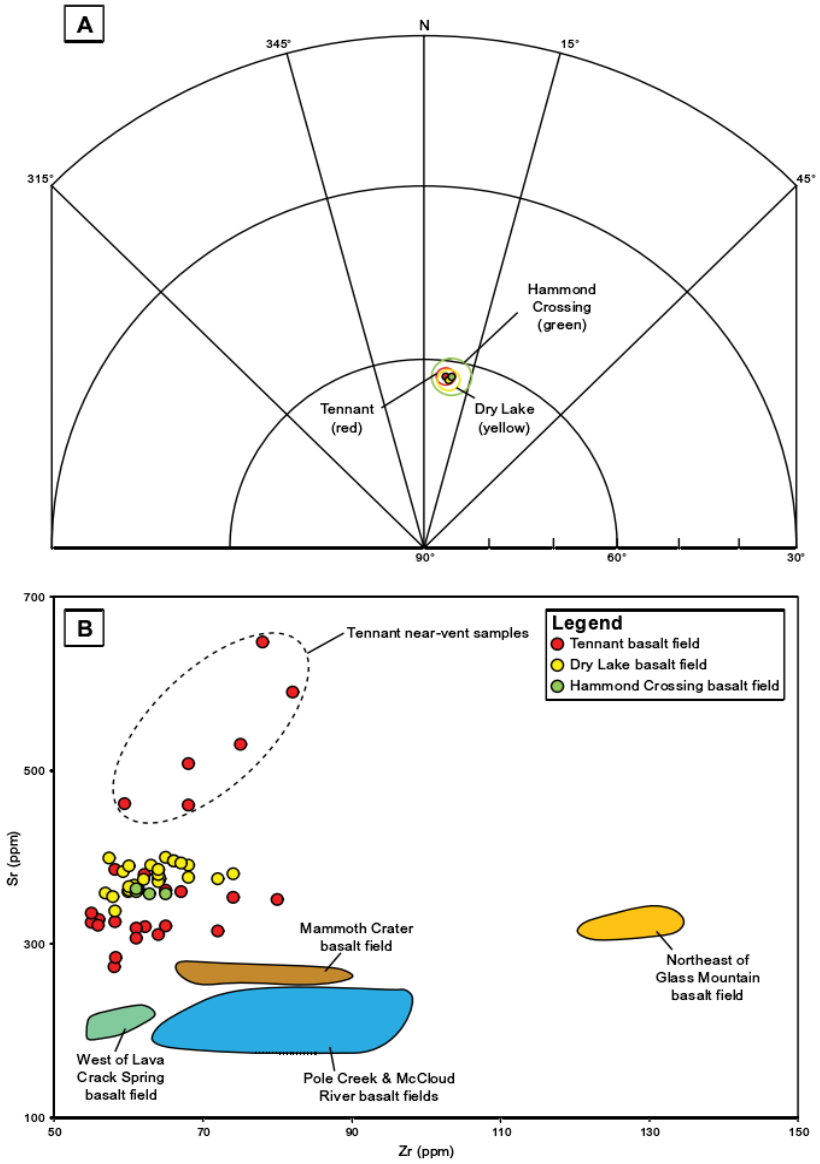

Figure 1. (A) Part of a lower-hemisphere equal-area stereographic projection displaying mean remanent magnetic directions and ovals of 95% confidence for the Tennant (red), Dry Lake (yellow), and Hammond Crossing (green) basalt fields in northern California (USA). See Table S1 (see footnote 1) for paleomagnetic data. (B) Trace-element plot (Sr versus Zr) for Tennant, Dry Lake, and Hammond basalt fields (Table S2) compared to other back-arc tholeiitic basalts near Mount Shasta and Medicine Lake volcano. There is overlap in some major and trace elements, but enough disparity over the suite of elements to define distinct lava flows. Pole Creek and McCloud River (Christiansen et al., 2017) overlap in almost all major and trace elements, but are distinct from other back-arc tholeiitic basalts. Data used to plot Mammoth Crater, northeast of Glass Mountain, and west of Lava Crack Spring, are from Donnelly-Nolan (2008). See Figure S5 for basalt locations.

4. 深海沉积物中逆磁化率结构:对磁小体丰度和排列的影响

翻译人:李园洁 liyj3@sustech.edu.cn

Usui, Y., Yamazaki, T., Oka, T., & Kumagai, Y. ***Inverse magnetic susceptibility fabrics in pelagic sediment: Implications for magnetofossil abundance and alignment. Journal of Geophysical Research: Solid Earth****, 2019, 124, 10,672–10,686. https://doi.org/10. 1029/2019JB018128*

摘要: 单畴磁铁矿颗粒在其拉长方向上显示出最小磁化率，从而导致磁化率各向异性（AMS）的所谓逆结构。本文从北太平洋西部约 12 m 长的活塞岩芯获得的深海粘土中发现了 AMS 逆结构。之前的研究确定了趋磁细菌(磁小体)产生的化石单畴磁铁矿是沉积物中主要的亚铁磁性矿物。在约 2 m 的区域发现逆 AMS 结构。在该区域之上约 6 和之下约 4 m 的沉积物显示出正常的水平 AMS 结构。岩石磁数据和铁磁共振光谱表明，不论正常或逆 AMS，磁小体占大多数平均磁化率。用混合模型可以解释了这一点，在这种模型中，磁小体的逆结构几乎与陆源矿物的正常结构保持平衡。据估计，沉积物中磁小体 S 携带的 AMS 的校正程度约为 1.01，这与典型的浅部深海沉积物的校正程度相当。另一方面，据估计，沉积物中的陆源矿物具有较高的各向异性度，可能反映埋藏和随后侵蚀的> 80 m 沉积物，这得到下层声学地层学的验证。这表明由于磁小体造成的逆 AMS 结构可能广泛分布在没有强力压实的深海粘土中。

ABSTRACT： Single-domain magnetite particles exhibit minimum susceptibility along their elongation, resulting in so-called inverse fabric of the anisotropy of magnetic susceptibility (AMS). We report the discovery of inverse AMS fabrics from pelagic clay recovered by a ~12 m long piston core from the western North Pacific. A previous study identified fossil single-domain magnetite produced by magnetotactic bacteria (magnetofossils) as the dominant ferrimagnetic mineral in the sediment. The inverse AMS fabrics were found in a ~2 m zone. The ~6 and ~4 m of sediment above and below this zone showed normal, horizontal AMS fabrics. Rock magnetic data and ferromagnetic resonance spectroscopy indicated that magnetofossils account for most of the mean susceptibility regardless of normal or inverse AMS. This was explained by the mixing models where the inverse fabric from magnetofossils is nearly balanced by the normal fabrics of

terrigenous minerals. The corrected degree of AMS carried by magnetofossils in the sediment was estimated to be ~1.01, which is comparable to that of typical pelagic sediment at shallow depth. On the other hand, terrigenous minerals in the sediment were estimated to have higher degree of anisotropy, possibly reflecting burial and subsequent erosion of >80 m of sediment, which was also suggested by a subbottom acoustic stratigraphy. This suggests that inverse AMS fabrics due to magnetofossils may be widespread in pelagic clay without strong compaction.

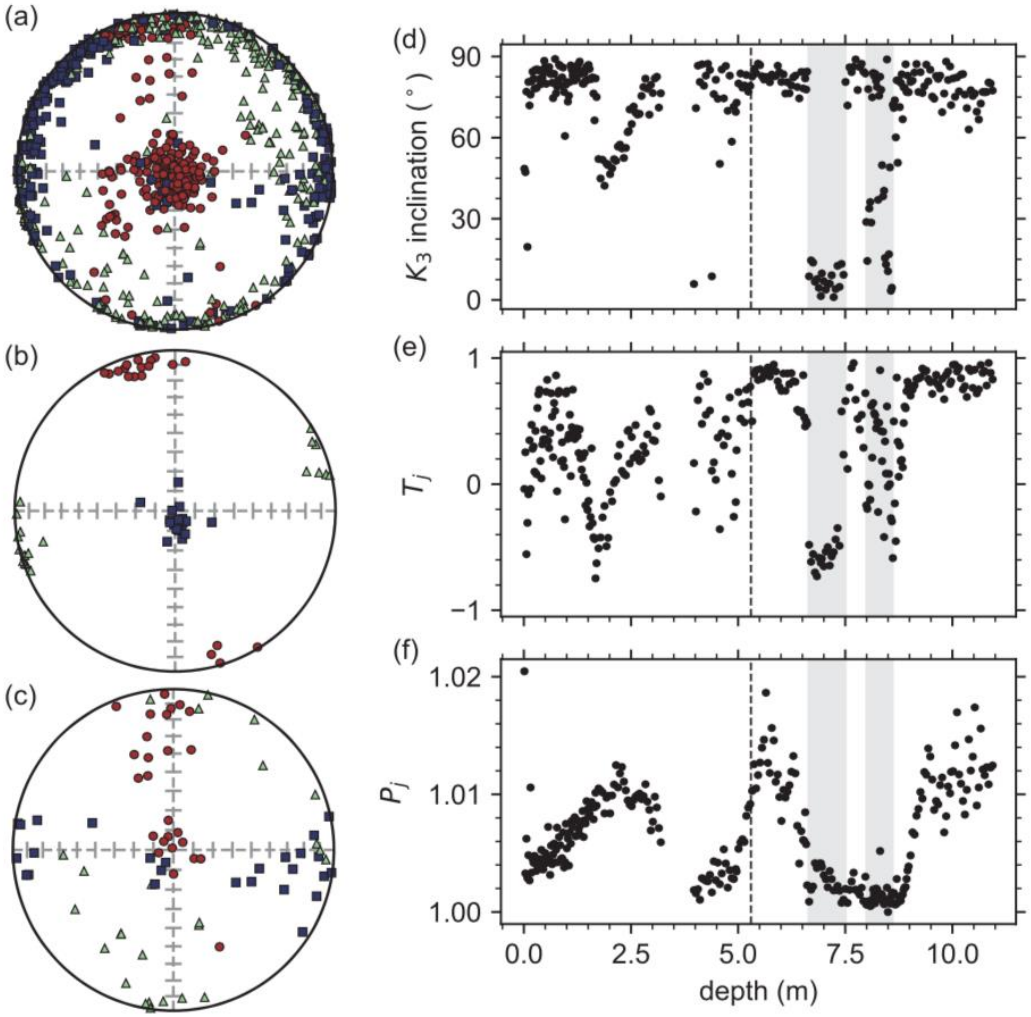

Figure 1. (a–c) Equal area projection of the principal AMS axes directions in core coordinates. Blue squares are K1, green triangles are K2, and red circles are K3. Panel (a) displays all data, (b) 6.65–7.5 m, and (c) 8–8.6 m. (d–f) Depth profile of AMS parameters. Shaded areas indicate the intervals with the inverse fabrics (6.65–7 and 8–8.6 m). Vertical dashed lines indicate the position of possible hiatus (Usui et al., 2017).

5. 48-40 ka 放射性碳时间尺度的扩展膨胀以及尼安德特人和智人的重叠时间

翻译人：柳加波 liujb@sustech.edu.cn

Bard E, Heaton T J, Talamo S, et al. Extended dilation of the radiocarbon time scale between 40,000 and 48,000 y BP and the overlap between Neanderthals and Homo sapiens[J]. Proceedings of the National Academy of Sciences, 2020.

https://doi.org/10.1073/pnas.2012307117

摘要：基于新的放射性碳校正曲线(IntCal20)，我们能够计算过去 55 ka 年间的 ^{14}C 年代和公元纪年之间的梯度。新的梯度曲线在 48-40ka ka BP 间具有持久和显著的最大值，并且在此期间，放射性碳时钟的运行速度几乎是其应有的两倍。这种放射性碳时间膨胀是由于，向 41 ka BP 左右的 Laschamp 漂移事件过渡期间，^{14}C 生产速率提高，并导致大气中 $^{14}C/^{12}C$ 比值的上升。IntCal20 校正曲线的一个新特征是 48 ka BP 到 40 ka BP 的出现的梯度最大值，这对该时间范围内要求精确年代的科学研究（如史前和古气候学）具有深远的影响。为了说明这一点，我们讨论了欧亚大陆中尼安德特人和智人之间重叠的持续时间。

ABSTRACT: The new radiocarbon calibration curve (IntCal20) allows us to calculate the gradient of the relationship between ^{14}C age and calendar age over the past 55 millennia before the present (55 ka BP). The new gradient curve exhibits a prolonged and prominent maximum between 48 and 40 ka BP during which the radiocarbon clock runs almost twice as fast as it should. This radiocarbon time dilation is due to the increase in the atmospheric $^{14}C/^{12}C$ ratio caused by the ^{14}C production rise linked to the transition into the Laschamp geomagnetic excursion centered around 41 ka BP. The major maximum in the gradient from 48 to 40 ka BP is a new feature of the IntCal20 calibration curve, with far-reaching impacts for scientific communities, such as prehistory and paleoclimatology, relying on accurate ages in this time range. To illustrate, we consider the duration of the overlap between Neanderthals and *Homo sapiens* in Eurasia.

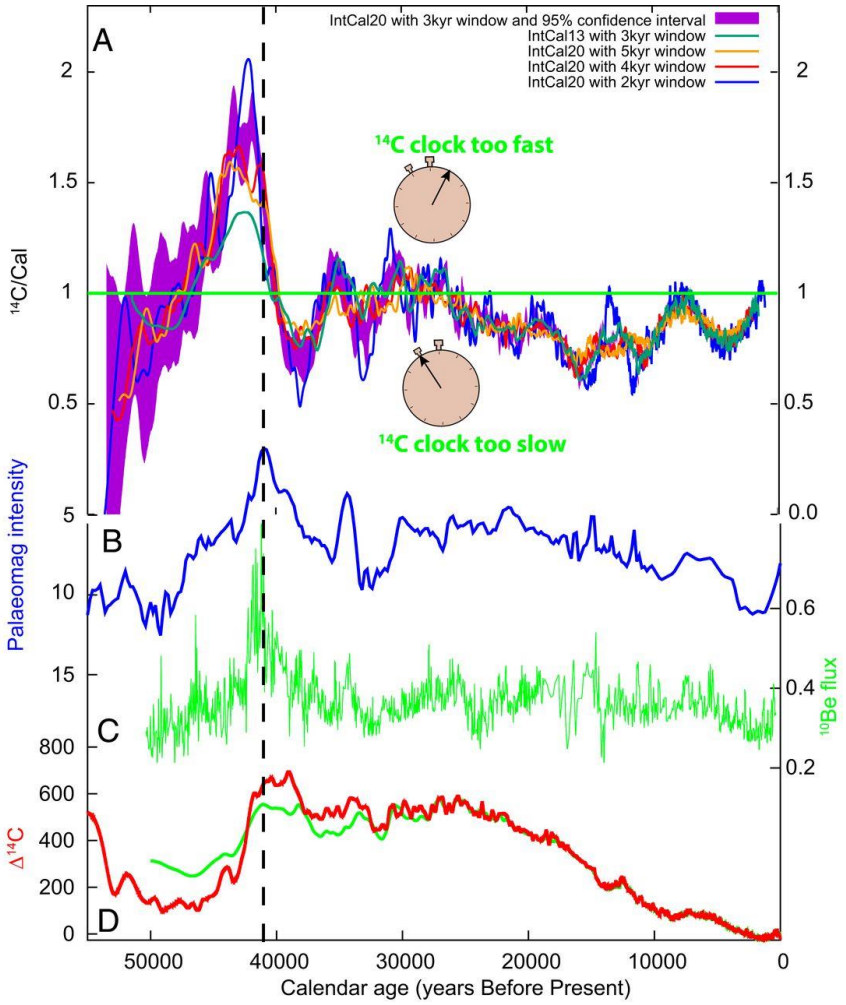

Fig 1: (A) First derivative of the IntCal20 curve (1) computed by calculating the 14C age vs. calendar age gradient over sliding windows of between 5,000- and 2,000-y durations. The purple area shows the 95% confidence interval for the 3,000-y window (to maintain legibility this is the only interval plotted). The green curve shows the first derivative of the IntCal13 curve (2) using the 3,000-y window (to be compared with the purple curve for IntCal20). When the gradient is above (below) unity, the 14C clock ticks faster (slower) than it should. (B) Evolution of the intensity (in 1022Am2) of the geomagnetic field (6); note the reversed scale. (C) The 10Be flux (in 106 atoms·cm−2·y−1) measured in Greenland ice cores (7). (D) Atmospheric Δ14C (in per mille above modern) based on the IntCal20 in red (1) and IntCal13 in green (2). The prominent maximum of the gradient curve (A) centered around 43 ka BP corresponds to the rising phase of the Δ14C curve (D) and thus predates the Δ14C and 10Be flux maxima (C) and the paleomagnetic intensity minimum (B) corresponding to the Laschamp geomagnetic excursion (vertical dashed line). (citations refer to original paper)

6. 南海西南次海盆构造主导的海底扩张---来自地震学的证据

翻译人：刘伟 inewway@163.com

Junhui Y , Pin Y , Yanlin W , et al. Seismic Evidence for Tectonically Dominated Seafloor Spreading in the Southwest Sub‐basin of the South China Sea[J]. Geochemistry Geophysics Geosystems, 2018, 19:3459-3477.

https://doi.org/10.1002/2015GC006113

摘要：海底扩张可以用不同的动力机制来解释，即以岩浆作用还是以构造作用为主导。西南次海盆位于南海海底扩张的西南端，由于对地壳结构的认识不足和存在争议，其扩张机制尚不清楚。本文对横跨西南次海盆地的两条多道地震线和一条海底地震仪线（OBS）进行了再处理和分析，以分析其地壳成像结构。结果显示沉积物在深海盆地上通常厚 0.5-1.0 km，在一些地堑中稍厚一些。在残留扩散中心发现了最厚(3.3km)的沉积物，其基底相当粗糙，并被普遍存在的地壳断裂高度切割。残留扩散中心的特征主要表现为中深谷，类似于岩浆扩散较差的情况。这两条多道地震线在破碎基底下 1.5- 到 3.6- 公里处都有一些间断和漫反射体。这些反射与 OBS 反演得到的速度 6.8-7.2 km/s 有很好的一致性，被解释为莫霍反射。因此，推测的地壳厚度不包括沉积物只有 1.5-3.6 km，比通常要薄得很多。而速度低于 8.0 km/s 的下伏地幔可能由于水沿这些地壳断层的渗透而被蛇纹石化。综上，认为西南亚盆地的扩张是构造主导的。

ABSTRACT: Seafloor spreading can be explained by different dynamic mechanisms, magmatically or tectonically dominated. The Southwest Sub‐basin, located at the southwest tip of the propagating seafloor spreading of the South China Sea, remains unclear for its spreading regime owing to poor and debated knowledge of the crustal structures. Here two multichannel seismic lines and one oceanic bottom seismometer line across this subbasin are reprocessed and analyzed with focus on crustal imaging. The sediments are usually 0.5–1.0 km thick over the abyssal basin and slightly thicker in the few grabens. The thickest (3.3 km) sediments are found in the fossil spreading center. The basement is fairly rough and highly faulted by ubiquitous crustal faults. The fossil spreading center is characterized by a deep median valley, similar to that of magma‐poor spreading cases. Both multichannel seismic

lines show a few intermittent and diffusive reflectors at 1.5 - to 3.6 - km depth below the fragmented basement. These reflectors, correlating well with the velocities of 6.8–7.2 km/s obtained from velocity inversion of oceanic bottom seismometer data, are interpreted as Moho reflections. Thus, the inferred crustal thickness is only 1.5–3.6 km excluding the sediments, which is much thinner than usual. The underlying mantle with velocities lower than 8.0 km/s might be serpentinized with water infiltration along these crustal faults. Therefore, it is proposed that the spreading of the Southwest Sub - basin was tectonically dominated.

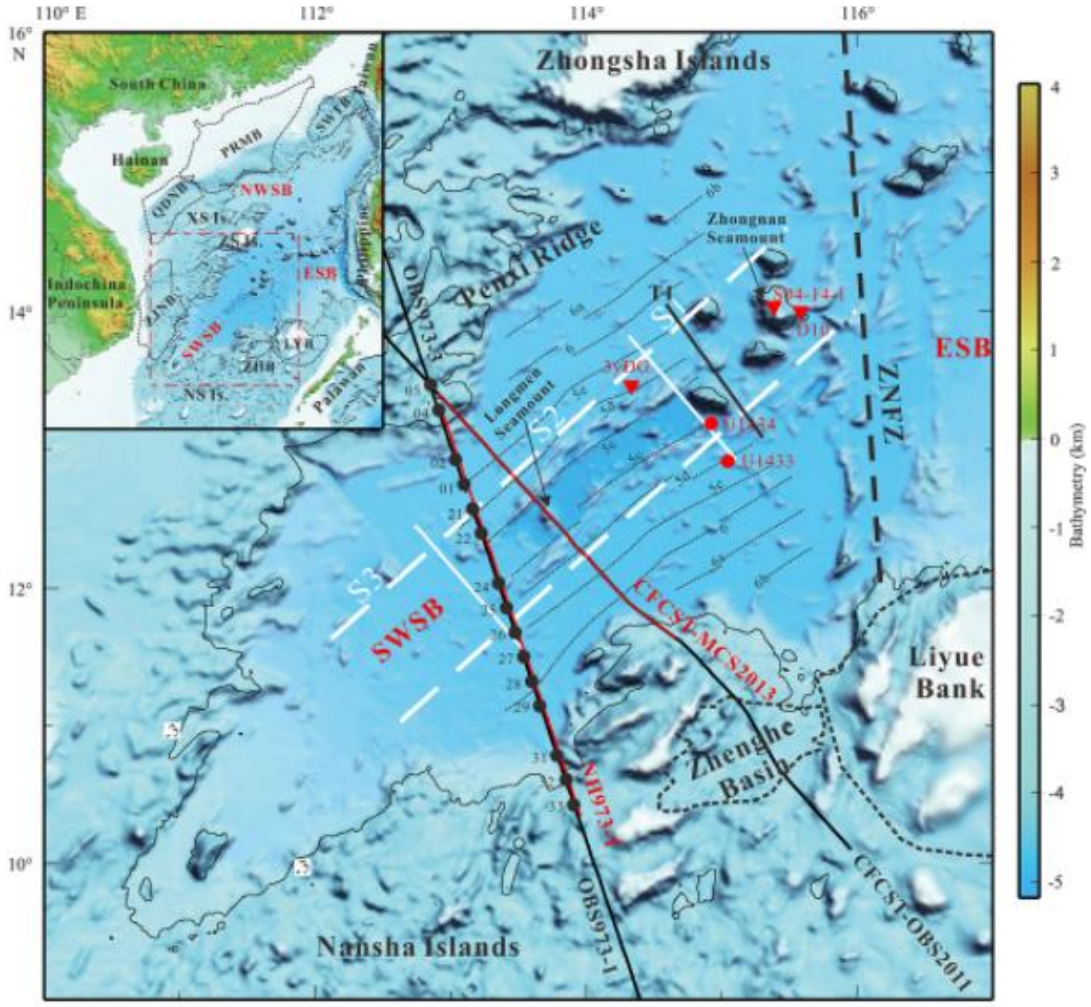

Figure 1. Bathymetric map of the Southwest Sub - basin of the South China Sea. The base map is from Yang et al. (2015). Inset shows location of the study area by red dashed box. The black lines indicate the oceanic bottom seismometer (OBS) lines: OBS973 - 1 (Qiu et al., 2011), OBS973 - 3 (Lü et al., 2011), CFCST - OBS2011 (Pichot et al., 2014), and T1 (Zhang et al., 2016). The red lines present the collocated multichannel seismic (MCS) sections (NH973 - 1 and CFCST - MCS2013) reprocessed in

this study. The black dots denote the OBS positions of line OBS973. Sites (U1433 and U1434) of International Ocean Discovery Program Expedition 349 are indicated by red dots. The red triangles indicate the dredge sites: 3yDG (Qiu et al., 2008), S04‐14‐1 and D10 (Yan et al., 2014). The thick black dashed line shows the boundary between the East Sub‐basin and the Southwest Sub‐basin. The magnetic lineations interpreted by Briais et al. (1993) are shown in thin black dashed lines. The fossil spreading center is sketched with white dashed lines. NWSB, the Northwest Sub‐basin; ESB, the East Sub‐basin; SWSB, the Southwest Sub‐basin; ZNFZ, Zhongnan Fracture Zone; XS Is., Xisha Islands; ZS Is., Zhongsha Islands; NS Is., Nansha Islands; SWTB, Southwest Taiwan Basin; PRMB, Pearl River Mouth Basin; QDNB, Qiongdongnan Basin; ZJNB, Zhongjiannan Basin; ZHB, Zhenghe Basin; LYB, Liyue Basin.

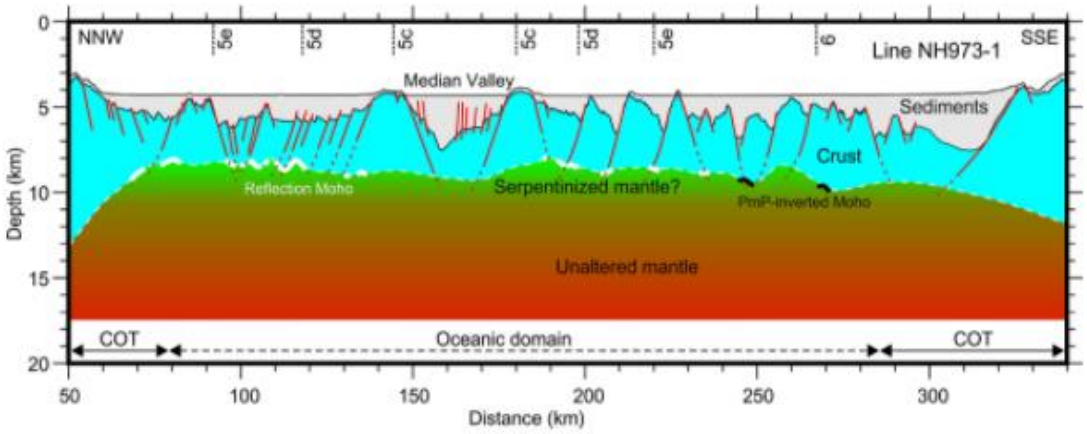

Figure 2. Schematic interpretation of the deep structure of the Southwest Sub‐basin along profile NH973‐1. The magnetic lineations interpreted by Briais et al. (1993) are shown in black dashed lines. The red lines indicate normal faults. The white thick lines represent the reflection seismic Moho from MCS profile NH973‐1, while the black thick lines indicate the PmP‐inverted Moho from the final model of OBS973.

7. 地中海地幔动力学的地形表现

翻译人：曹伟 11930854@QQ.com

Claudio F., Thorsten W. B. Topographic expressions of mantle dynamics in the Mediterranean [J]. Earth-Science Reviews, 2020: 103327

https://doi.org/10.1016/j.earscirev.2020.103327

摘要：地表形态是发生在地球表面或深部的动态过程不断变化的表现。然而，我们根据潜在的构造或气候动力来“解读”地貌的能力仍然处于初级阶段。在过去的十年中，深部动力对地表的影响受到了广泛关注，尤其是关于岩石圈底部地幔对流产生的应力，以及它们与地形（iso）静态分量的相关性。本研究中，我们使用来自地中海的例子来估计残差和动态地形，然后我们将其与特定区域的地质地表隆起进行比较，以区分动态和静态成分。通过考虑构造过程的不同地形特征(如实际地形、残余地形和动态地形以及上升速率)，共同提供了一种区分地幔、地壳和表面过程的有效方法。这种方法可能使我们更接近于从地质原因来解读地表现象。

ABSTRACT: The surface of the Earth is the ever-changing expression of the dynamic processes occurring at depth and at or above its surface. However, our ability to “read” landscapes in terms of their underlying tectonic or climatic forcing remains rudimentary. During the last decade, particular attention has been drawn to the deep dynamic contributions to topography, related to the stresses that are produced at the base of the lithosphere by mantle convection, and their relevance compared to the (iso)static component of topography. Here, we use examples from the Mediterranean and estimate residual and dynamic topography. We then compare those with surface uplift from geology for specific regions to disentangle the dynamic from the static components. Considering the different topographic signatures of tectonic processes (e.g. actual, residual, and dynamic topography as well as uplift rates) jointly provides a powerful way to distinguish between the contributions of mantle, crustal, and surface processes. Such an approach might bring us closer to reading topographic expressions in terms of their geological cause.

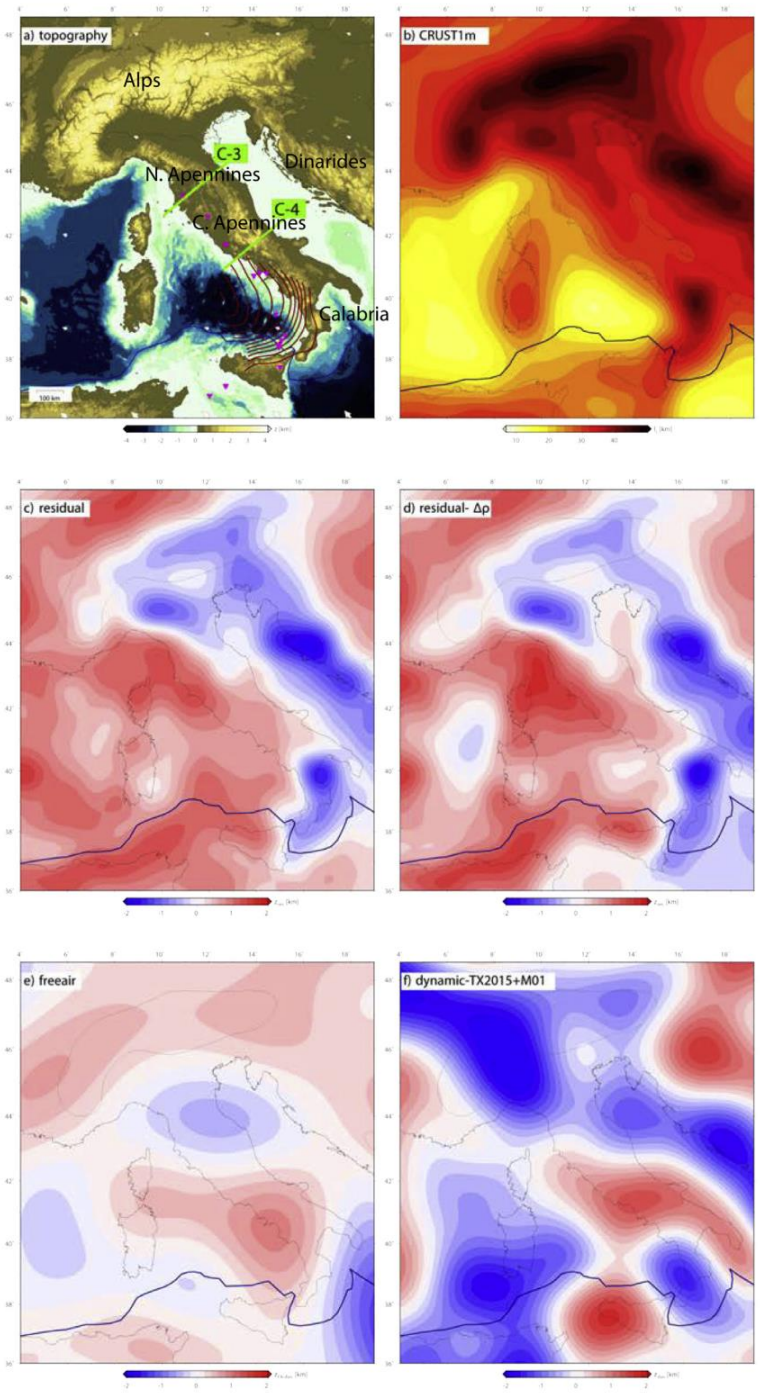

Figure 1. Central Mediterranean topography (a). Crustal thickness is from an updated merger of regional datasets and CRUST1 (b) used to estimate residual topography using constant density (c) or with crustal density variation from CRUST1 (d) (as in Fig. 3a and b). Dynamic (non-compensated) topography estimated from filtered free air gravity anomalies using the "admittance" scaling as in Craig et al. (2011) (e, as in Fig. 3c) and dynamic topography as in Fig. 4c.

8. 中国中部过去千年的水汽变化及其与热带太平洋和北大西洋的联系

翻译人：杨会会 11849590@mail.sustech.edu.cn

Duan F C, Zhang Z Q, Wang Y et al. Hydrological variations in central China over the past millennium and their links to the tropical Pacific and North Atlantic oceans[J].Climate of the Past, 2020,16,475-485

https://doi.org/10.5194/cp-16-475-2020

摘要：东亚夏季风(EASM)区近一千年来的降水变化，也称为“梅雨”，可能有助于启发对未来全球变暖的水文响应。本文从中国中部永兴洞获得了一个具有精确年代和高分辨率的石笋 $\delta^{18}O$ 记录。我们的新记录，结合之前发表的同一洞穴的记录，表明梅雨与全球气温变化有显著的关联。特别地，我们的记录显示梅雨在中世纪气候异常(MCA)期间减弱，而在小冰期(LIA)期间增强。在当前的暖期(CWP)，我们的记录显示梅雨也有类似的减弱。此外，我们的记录显示，在 MCA 和 CWP 期间，中国北方的大气降水一样湿润，而中部的大气降水一样干燥，但在 CWP 期间，中国南方的大气降水相对湿润。这种空间差异表明了区域降水对人为作用的复杂局部响应。在 MCA (LIA)期间减弱(增强)的梅雨与北半球表面空气温度的暖(冷)相吻合。这种梅雨模式也很符合热带印度太平洋暖池的气候状况。另一方面，我们的记录也显示了与北大西洋气候的紧密联系。梅雨的减少(增加)与北大西洋振荡的正(负)阶段有很好的相关性。此外，我们的记录与 MCA (LIA)期间大西洋经向翻转环流的强(弱)有很好的联系。上述数十年-百年尺度的局部联系和遥相关表明梅雨与 MCA 和 LIA 期间热带太平洋和北大西洋的海洋过程密切相关。

ABSTRACT: Variations of precipitation, also called the Meiyu rain, in the East Asian summer monsoon (EASM) domain during the last millennium could help enlighten the hydrological response to future global warming. Here we present a precisely dated and highly resolved

stalagmite $\delta^{18}O$ record from the Yongxing Cave, central China. Our new record, combined with a previously published one from the same cave, indicates that the Meiyu rain has changed dramatically in association with the global temperature change. In particular, our record shows that the Meiyu rain was weakened during the Medieval Climate Anomaly (MCA) but intensified during the Little Ice Age (LIA). During the Current Warm Period (CWP), our record indicates a similar weakening of the Meiyu rain. Furthermore, during the MCA and CWP, our records show that the atmospheric precipitation is similarly wet in northern China and similarly dry in central China, but relatively wet during the CWP in southern China. This spatial discrepancy indicates a complicated localized response of the regional precipitation to the anthropogenic forcing. The weakened (intensified) Meiyu rain during the MCA (LIA) matches well with the warm (cold) phases of Northern Hemisphere surface air temperature. This Meiyu rain pattern also corresponds well to the climatic conditions over the tropical Indo-Pacific warm pool. On the other hand, our record shows a strong association with the North Atlantic climate as well. The reduced (increased) Meiyu rain correlates well with positive (negative) phases of the North Atlantic Oscillation. In addition, our record links well to the strong (weak) Atlantic meridional overturning circulation during the MCA (LIA) period. All abovementioned localized correspondences and remote teleconnections on decadal to centennial timescales indicate that the Meiyu rain was coupled closely with oceanic processes in the tropical Pacific and North Atlantic oceans during the MCA and LIA.

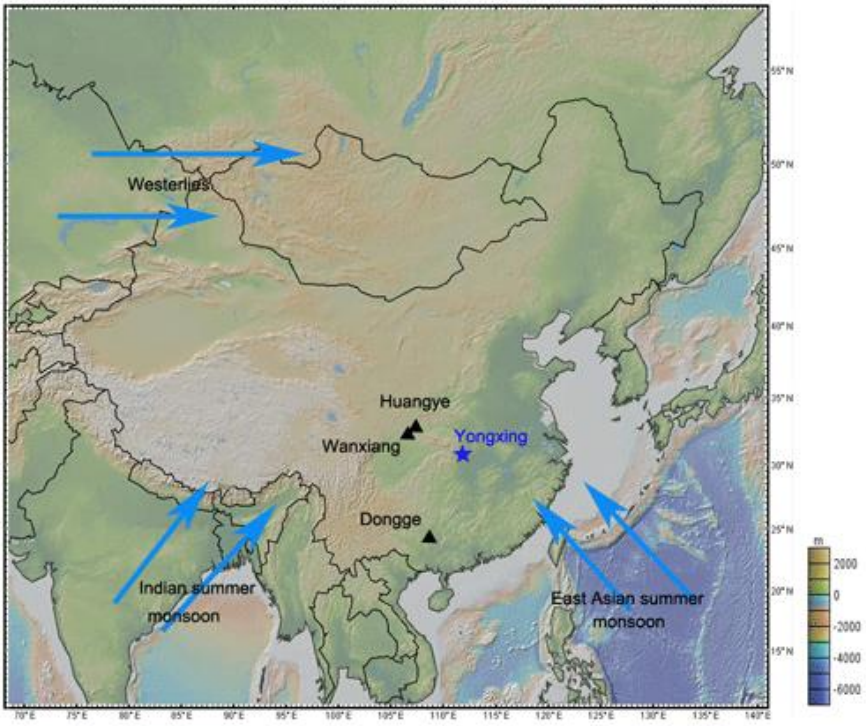

Figure 1. A schematic climate setup of East Asian monsoon systems and our study site. This figure was made with GeoMapApp (http://www.geomapapp.org, last access: 12 January 2020). The blue star and black triangles represent Yongxing Cave in central China and other caves in the monsoonal region, respectively.

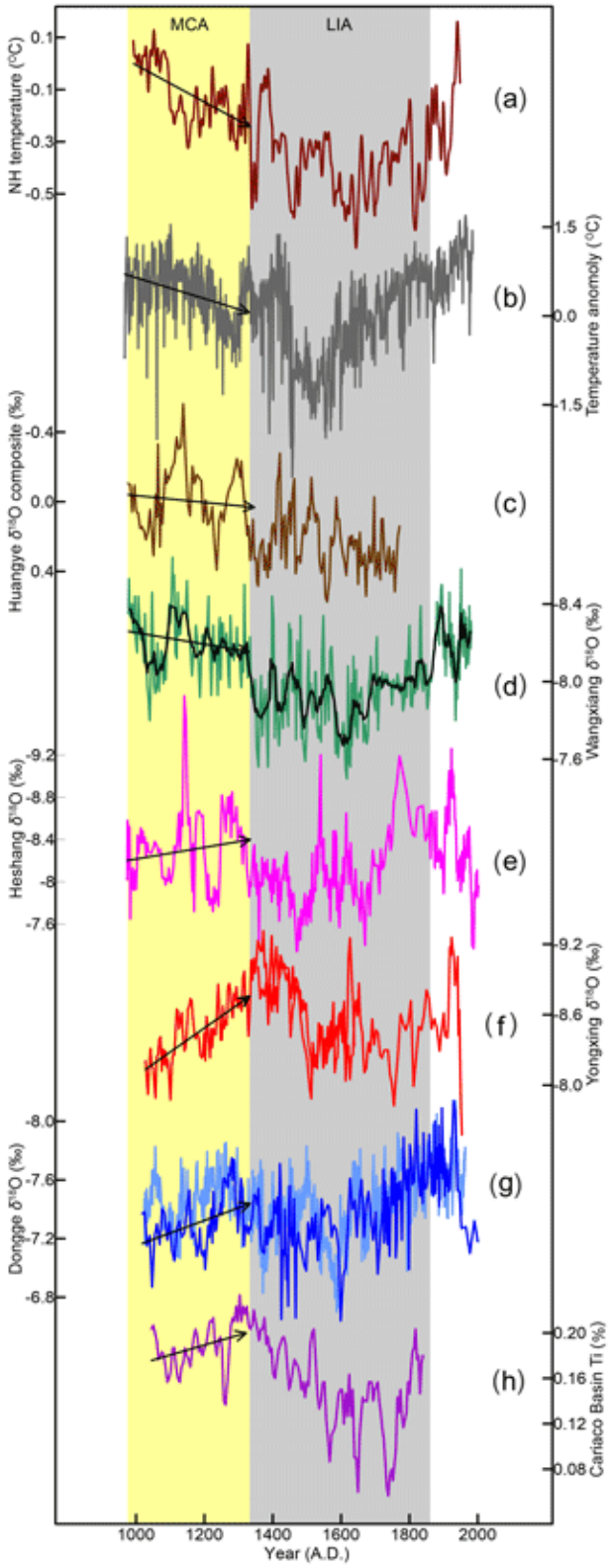

Figure 2. A comparison of the Yongxing $\delta^{18}O$ time series with other proxy records. **(a)** Northern Hemisphere reconstructed temperature (Mann et al., 2009); **(b)** northern China reconstructed temperature (Tan et al., 2003); **(c)** Huangye Cave $\delta^{18}O$ composite (Tan et al., 2011b); **(d)** Wanxiang

Cave $\delta^{18}O$ record (Zhang et al., 2008); **(e)** Heshang Cave $\delta^{18}O$ record (Hu et al., 2008); **(f)** Yongxing Cave record (this study); **(g)** Dongge Cave record (Wang et al., 2005; Zhao et al., 2015); **(h)** Cariaco Basin Ti content record (Haug et al., 2001). Light yellow and blue bars indicate the MCA and LIA, respectively. Arrows, constrained by linear fit methods, indicate trends of the climatic variations.

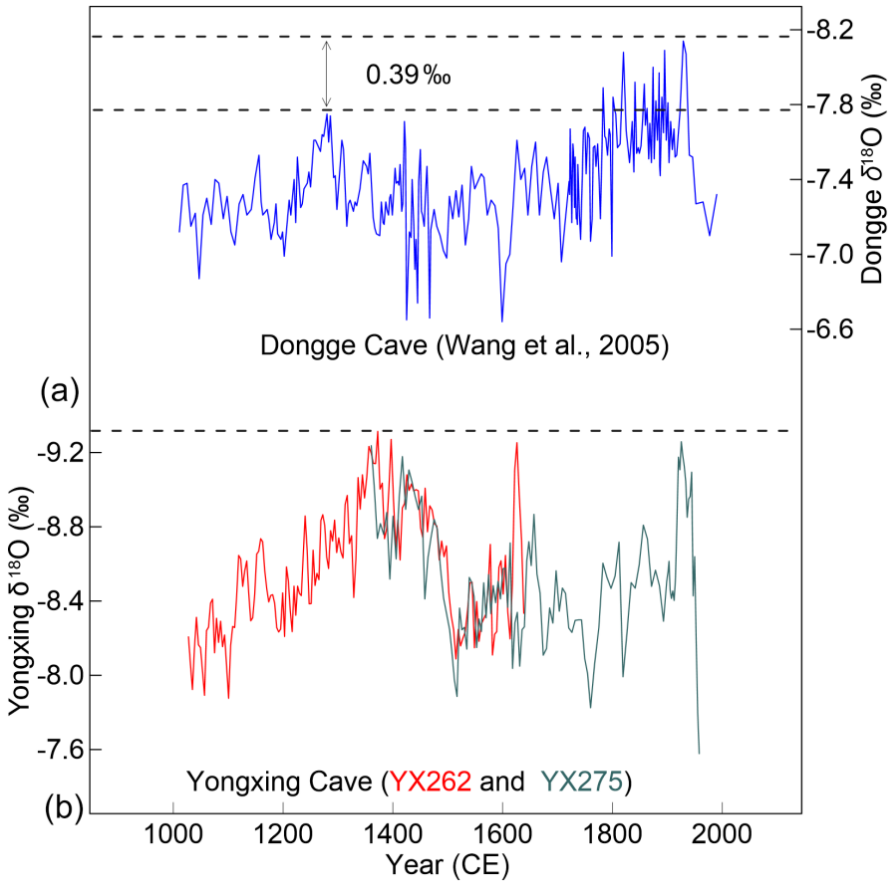

Figure 3. The relative intensity of Meiyu rain during the MCA compared to the CWP. **(a)** The Dongge Cave record (blue curve; Wang et al., 2005); **(b)** the Yongxing Cave YX262 (red curve) and YX275 (green curve; W. Zhang et al., 2019) records. On average, the Dongge Cave record shows a 0.39 ‰ lower $\delta^{18}O$ value during the CWP than the MCA. However, the Yongxing record shows a comparable value between the CWP and MCA.

9. 全球风尘循环和大洋铁输入

翻译人：王敦繁 dunfan-w@foxmail.com

Natalie M. Mahowald et. Atmospheric global dust cycle and iron inputs to the ocean[J]. Global Biogeochem. Cycles, 2005, 19(4).

https://doi. 10.1029/2004GB002402, 2005

摘要：由于铁是一种重要的微量元素，风尘中的铁进入大洋会影响碳循环和大气中的二氧化碳。本文回顾了我们目前对全球风尘循环的理解，并确定了未来的研究重点。全球沙漠风尘的分布是根据对来自现场浓度、光学深度和沉积数据的观测组合估计的;这些数据数据主要来自卫星观测;以及全球大气模型。人类活动影响的大气风尘通量被认为比自然影响的要小，但是由于对沙尘、气候、土地利用和水资源利用变化的反应了解不足，因此难以量化。气溶胶的铁含量被认为大约有 2 倍的变化，而在某些地区，由于高度的空间和时间变异性和有限的观测，风尘沉降的不确定性至少有 10 倍。更重要的是，在大气输送过程中，相对不溶性的土壤铁(通常为 0.5%的可溶性)变得更加可溶性(1-80%)，我们对这一过程的了解还很有限，但这些过程可能受到人为排放的硫或有机酸的影响。为了理解人类将如何影响未来海洋中的铁沉积,我们需要提升以下方面的认识:风尘铁在偏远海洋中的沉积,风尘铁在气溶胶中的化学行为,风尘来源是如何响应气候变化的,和人类活动将如何影响海洋中生物可利用的铁的传输。

ABSTRACT: Since iron is an important micronutrient, deposition of iron in mineral aerosols can impact the carbon cycle and atmospheric CO2. This paper reviews our current understanding of the global dust cycle and identifies future research needs. The global distribution of desert dust is estimated from a combination of observations of dust from in situ concentration, optical depth, and deposition data; observations from satellite; and global atmospheric models. The anthropogenically influenced portion of atmospheric desert dust flux is thought to be smaller than the natural portion, but is difficult to quantify due to the poorly understood response of desert dust to changes in climate, land use, and water use. The iron content of aerosols is thought to vary by a factor of 2, while the uncertainty in dust deposition is at least a factor of 10 in some regions due to

the high spatial and temporal variability and limited observations. Importantly, we have a limited understanding of the processes by which relatively insoluble soil iron (typically ~0.5% is soluble) becomes more soluble (1 – 80%) during atmospheric transport, but these processes could be impacted by anthropogenic emissions of sulfur or organic acids. In order to understand how humans will impact future iron deposition to the oceans, we need to improve our understanding of: iron deposition to remote oceans, iron chemistry in aerosols, how desert dust sources will respond to climate change, and how humans will impact the transport of bioavailable fraction of iron to the oceans.

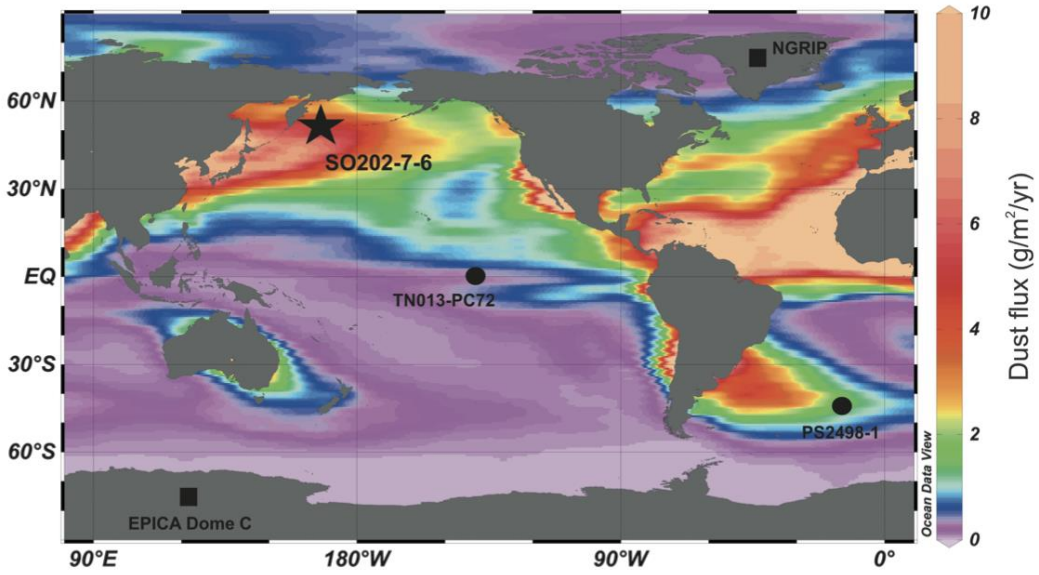

Figure 1.Desert dust deposition (g/m2/yr) estimated from an average of three reanalysis based models simulated for 10+ years [Luo et al., 2003; Ginoux et al., 2004; Tegen et al., 2004], and representing our best estimate of dust deposition. Models compare well to available in situ and satellite observations and are shown here compared against sediment trap data [Kohfeld and Harrison, 2001].

10. 中国中部新石器时代晚期的高可信度的古强度结果

翻译人：王浩森 11930841@mail.sustech.edu.cn

CAI S H, TAUXE L, WANG W L, et al. 2020. ***High-Fidelity Archeointensity Results for the Late Neolithic Period From Central China. Geophysical Research Letters [J], 47: 11.***

Doi: 10.1029/2020GL087625

摘要：古地磁学的重点是探索数百到数千年来地磁场的高分辨率变化。在这项研究中，我们对中国中部新石器时代晚期遗址的绝对古强度和相对古强度进行了全面研究。样本的年龄被限制在大约 3,500–3,000 BCE，这是一个可用的古强度数据较缺乏的时期。我们一共得到了 64 个高质量的绝对古强度，这些样品表明在大约公元前 3500 至 3,000 年之间，该场的在 55 ∽90 ZAm^2 范围内快速变化。我们的结果记录到大约 3300 BCE 的一个新的 jerk 事件，这可能是非偶极子场所导致的。新的地磁结果为全球地磁模型提供了进一步的约束条件。同时，绝对古强度和相对古强度随深度的变化显示出良好的一致性，从而加强了本文结果的可靠性。结合绝对古强度和相对古强度的这一新方法为未来的地磁研究提供了可靠帮助。

ABSTRACT: Archeomagnetism focuses on exploring high‐resolution variations of the geomagnetic field over hundreds to thousands of years. In this study, we carried out a comprehensive study of chronology, absolute and relative paleointensity on a late Neolithic site in central China. Ages of the samples are constrained to be ~3,500–3,000 BCE, a period when available paleointensity data are sparse. We present a total of 64 high‐fidelity absolute paleointensities, demonstrating the field varied quickly from ~55 to ~90 ZAm2 between ~3,500–3,000 BCE. Our results record a new archeomagnetic jerk around 3,300 BCE, which is probably non‐dipolar origin. The new results provide robust constraints on global geomagnetic models. We calculated a revised Chinese archeointensity reference curve for future application. The variations of absolute and relative paleointensity versus depth show good consistency, reinforcing the reliability of our results. This new attempt of combining absolute and relative paleointenstiy

provides a useful tool for future archeomagnetic research.

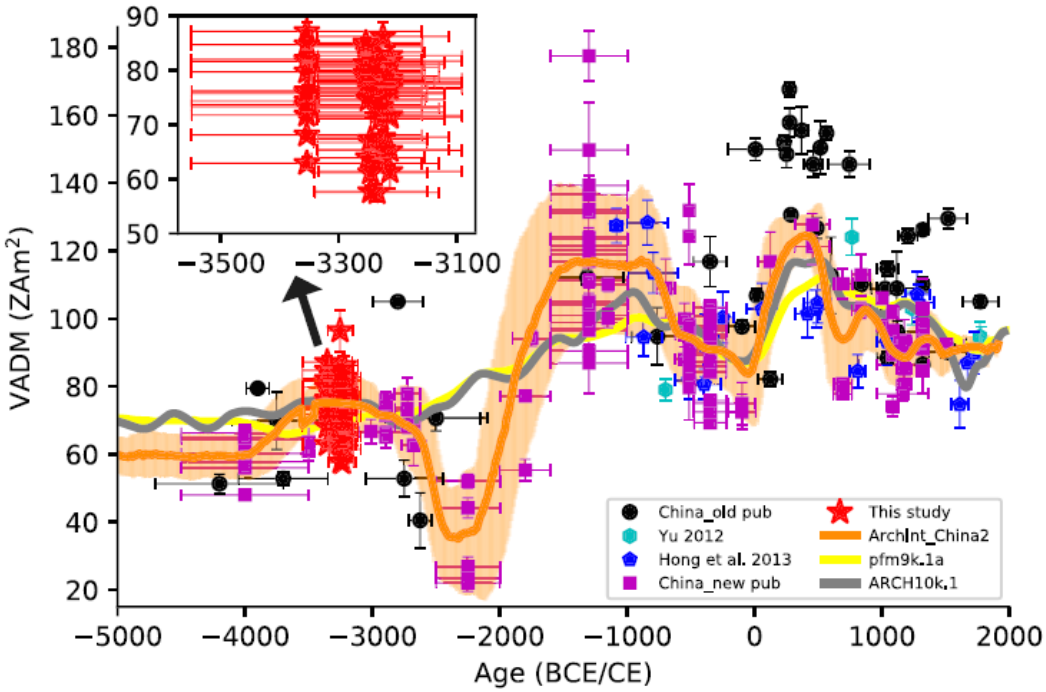

Figure 4. Comparison of VADMs in this study to published data in eastern Asia and predictions from global models. Red stars are data from this study. Amplified plot is shown as insert. Black solid circles are data published in the 1980s and 1990s after selection. Purple squares are our reanalyzed data published in recent years since 2014. Cyan hexagons/blue pentagons are published data in Japan (Yu, 2012)/Korea (Hong et al., 2013) in recent years. The gray and yellow lines are predictions from global models of ARCH10k.1 (Constable et al., 2016) and pfm9k.1a (Nilsson et al., 2014) at the center of China (35°N, 105°E). The orange line is the updated Chinese archeointensity reference curve.

11. 晚更新世中亚伊犁盆地火迹与古气候变化和人类活动之间的潜在联系

翻译人：郑威　11930589@mail.sustech.edu.cn

B Y M A , D Y S C , C Y L , et al. Late Pleistocene fire in the Ili Basin, Central Asia, and its potential links to paleoclimate change and human activities[J]. Palaeogeography, Palaeoclimatology, Palaeoecology, 547.

https://doi.org/10.1016/j.palaeo.2020.109700

摘要：中亚地区火的活动的证据对于理解火的潜在过程和控制因素很重要。这里展示了在伊利盆地的两个7万年来的黄土剖面发现的两个微木炭记录。结果显示在两个记录中总微木炭含量相似，并且记录与太阳辐射有关，说明了盆地范围内持续的火的活动趋势与太阳辐射驱动的水汽变化有关；另外，有两个火的异常活动事件发生在45到35前年前和6到0前年前。我们认为这些事件相较于自然因素（例如沉积，风，埋藏变化或气候变化），可能与古人类活动更有关。

ABSTRACT：Evidence of late Pleistocene fire activity in Central Asia is important for understanding the underlying processes and controls of fire. Here, two microcharcoal records from two separate loess sections covering the last ~70 thousand years (kyr) in the Ili Basin are reported. The results show that total microcharcoal concentrations are similar in both records and are correlated with insolation, indicating consistent basin-wide fire trends related to moisture changes driven by insolation; in addition, two anomalous fire events were identified at 45-35 ka and 6-0 ka. We argue that these events are possibly related to ancient human activities, rather than to pure natural factors such as sedimentation, wind, taphonomic change or climate change.

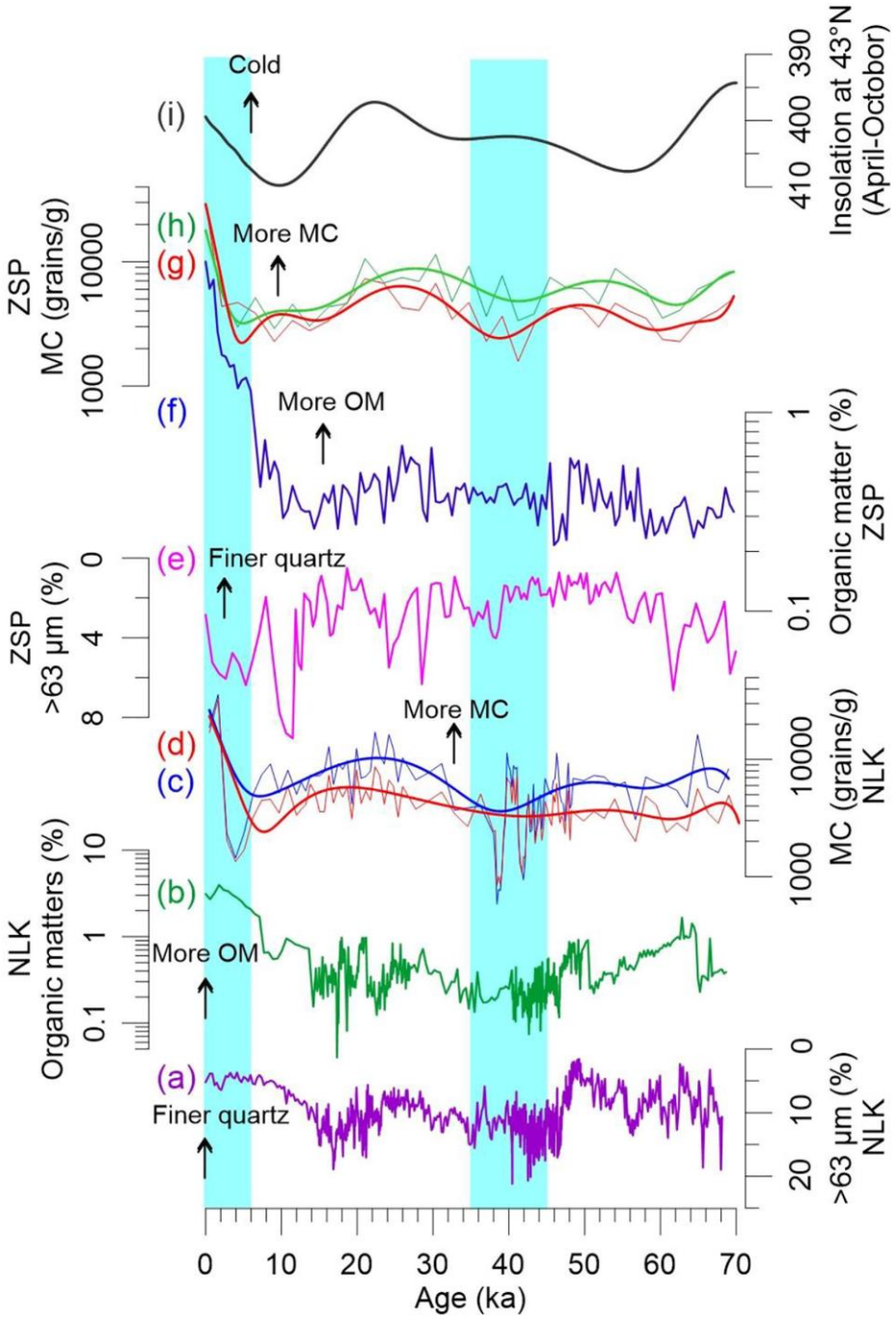

Figure 1. Comparisons of (a) grain size > 63μm, (b) organic matter, (c) MCL and (d) MCR in the NLK section; (e) grainsize > 63μm, (f) organic matter, (g) MCL and (h) MCR in the ZSP section; (i) insolation at 43°N during the plant growing season (smoothed curves in c, d, g and h are 10th-degree polynomials generated by Grapher 10.0; shallow blue rectangles indicate two periods of anomalous fire events. (For interpretation of the references to colour in this figure legend, the reader is referred to the web version of this article.)

12. 气泡对玄武岩熔岩流流变学的影响:大规模两相实验的启示

翻译人：张伟杰 12031188@mail.sustech.edu.cn

Soldati A, Farrell JA, Sant C, Wysocki R, Karson JA. ***The effect of bubbles on the rheology of basaltic lava flows: Insights from large-scale two-phase experiments****. EARTH PLANET SC LETT. 2020,548:116504.*

https://doi.org/10.1016/j.epsl.2020.116504

摘要：气泡对熔岩流变学有显著的影响，但是气泡对熔岩流流动距离的影响还没有被充分研究。为了定量气泡对熔岩流就位的影响，我们进行了一系列大尺度的两相（熔体+气泡）实验。在本研究中，9 个具有低到中度气泡含量（大约 3-24%）玄武岩熔岩流在具有轻微倾斜（4°-9°）的干砂表面就位。岩浆的流速通过粒子图像测速测定，用 Jeffreys 方程计算了它们的体积粘度。与没有气泡的纯的熔体进行对比，确定气泡对熔体黏度的影响。我们发现，在研究的孔隙度变化范围内，气泡增加了一个数量级的实验流动的相对粘度。我们的研究结果定量的评估了气泡对玄武质岩浆流变学性质的影响，将为改进多相流模型提供基础，而多相流模型是准确预测熔岩流位置的基础。

ABSTRACT: Bubbles are known to have a dramatic effect on lava rheology, but their impact on lava flow run out distance has not been extensively investigated. To quantify bubble effects on basaltic lava flow emplacement, we conducted a series of large-scale two-phase (melt+bubbles) experiments at the Syracuse University Lava Project facility. In this study, nine basaltic lava flows with low to intermediate vesicle contents (approximately 3-24vol%) were emplaced over gently sloping (4◦-9◦) dry sand surfaces. Their velocities were measured by particle image velocimetry, and their bulk viscosities were calculated using Jeffreys' equation. Comparison with melt-only viscosities (calculated through the GRD model) allowed the isolation of the effect of bubbles on the viscosity of the experimental flows. We find that within the investigated range of vesicularities, bubbles increase the relative viscosity of the experimental flows by up to an order of magnitude. The increase appears to be steeper for sheet flows than for lobate and toey flows. Our results, which quantitatively assess the effect of bubbles on the rheology of basaltic lava flows, will

provide a basis for the refinement of models for multi-phase flows that are fundamental to accurately forecasting the emplacement of lava flows.

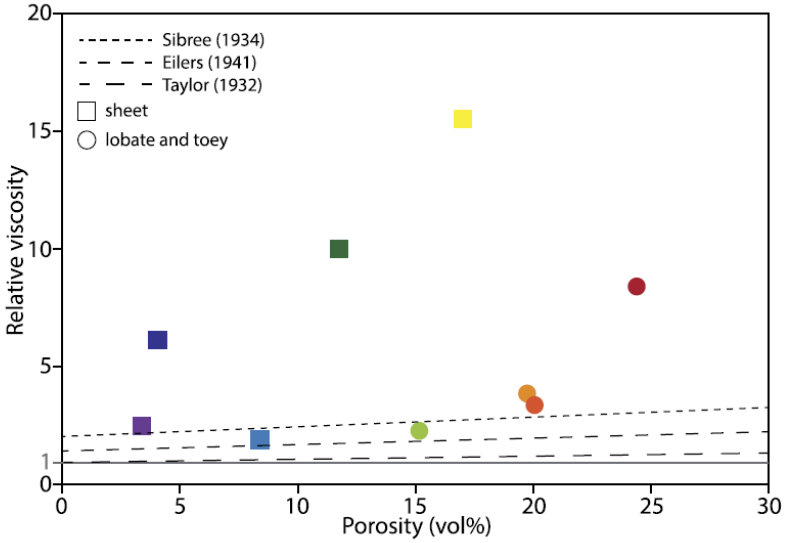

Figure 1. Correlation between lava relative viscosity and porosity. Three existing mod-els are plotted: Sibree (1934), Eilers (1941), and Taylor (1932). Color scheme corre-sponds to total vesicularity. Square symbols represent toey and lobate flows; circular symbols represent sheet flows.

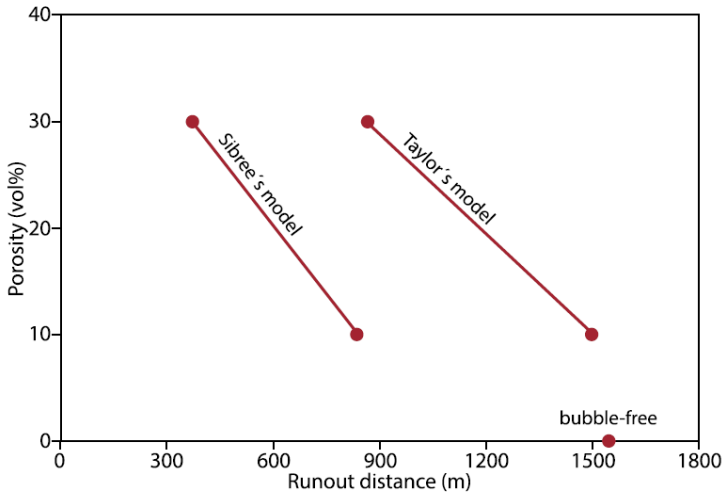

Figure 2. Modeled runout distance as a function of porosity for three example flows: a bubble-free flow, and two flows with porosities of 10 vol% and 30 vol%. Modeled runout distances are based on FLOWGO (Harris and Rowland, 2001), and as such they incorporate the effect of crystals. For the two bubble-bearing flows, FLOWGO (Harris and Rowland, 2001) is modified to account for porosity according to either Taylor's Law (Taylor, 1932) and Sibree's Law (Sibree, 1934).

13. 末次冰期气候突变事件的时间同步性

翻译人：李海 12031330@mail.sustech.edu.cn

Corrick, E. C., et al. (2020). "Synchronous timing of abrupt climate changes during the last glacial period." Science 369(6506): 963-969.

摘要：全球的古气候记录中已发现末次冰期的气候突变事件，但是我们对它们发生的绝对时间和区域同步性的理解不全。 我们对 63 个已发表且年代准确的石笋记录进行研究，发现格陵兰的突然变暖与亚洲季风、南美季风和欧洲-地中海地区的同步气候变化存在同步性。加上大气响应中双极同步的证明，这提供了在这些突然变暖期间气候变化的高纬度到热带同步耦合的独立证据。 我们的结果提供了一个全球一致的框架，可用来验证突变的气候变化的模型并限制冰芯的年代。

Abstract Abrupt climate changes during the last glacial period have been detected in a global array of palaeoclimate records, but our understanding of their absolute timing and regional synchrony is incomplete. Our compilation of 63 published, independently dated speleothem records shows that abrupt warmings in Greenland were associated with synchronous climate changes across the Asian Monsoon, South American Monsoon, and European-Mediterranean regions that occurred within decades. Together with the demonstration of bipolar synchrony in atmospheric response, this provides independent evidence of synchronous high-latitude–to-tropical coupling of climate changes during these abrupt warmings. Our results provide a globally coherent framework with which to validate model simulations of abrupt climate change and to constrain ice-core chronologies.

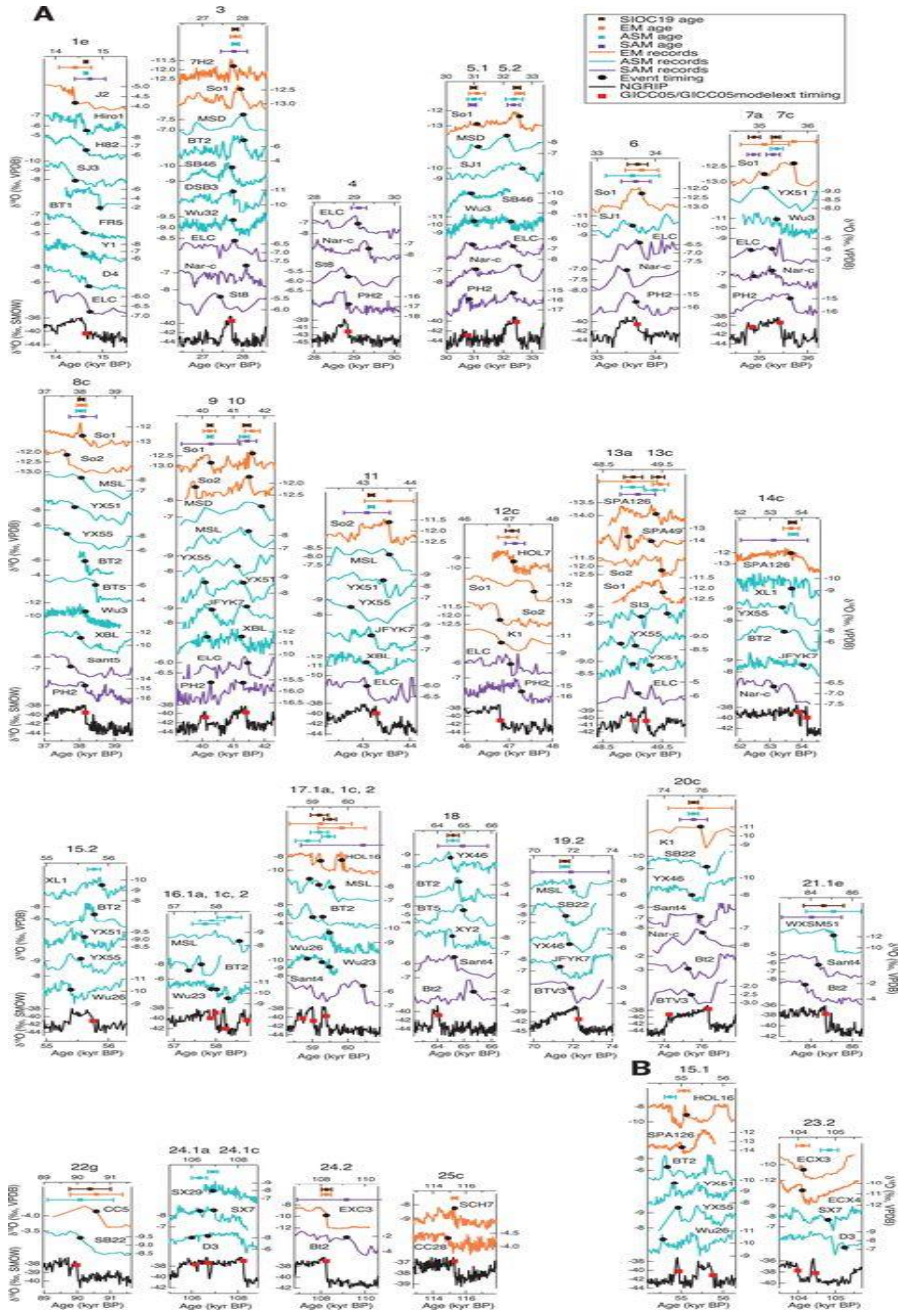

Figure 1. Stable isotope records of individual speleothems for each interstadial onset. (A and B) Each speleothem record displayed has met screening and event identification criteria (34) and is color-coded according to region (EM, orange; ASM, blue; and SAM, purple). All records are plotted on the recalculated chronology (34). Plots are provided for interstadial onsets found to be (A) synchronous and (B) nonsynchronous. (A) includes interstadials for which we have data from only one region. The North Greenland Ice Core Project (NGRIP) δ18O series on the GICC05 or GICC05modelext chronology is plotted in black, with each event position (3) indicated with a red square. The corresponding event position in each speleothem record is indicated with a solid black circle (timing

and uncertainty are provided in data file S1). Markers with error bars at the top of (A) and (B) indicate the age and 2σ uncertainty of the interregional age estimate (brown) and intraregional age estimates (EM, orange; ASM, blue; and SAM, purple). Lettering provides the name of each speleothem record. The full details and original reference for each record are provided in table S1. VPDB, Vienna Pee Dee belemnite; SMOW, standard mean ocean water; kyr, thousand years.

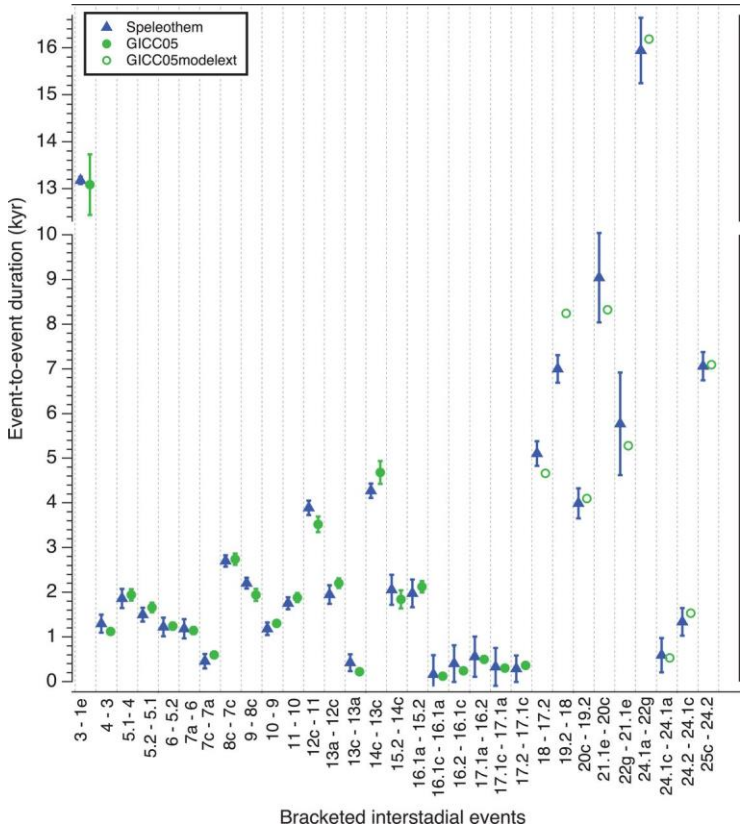

Figure 2. Years between the onset of consecutive interstadials. The time interval between the onset of consecutive interstadials in the GICC05/GICC05modelext chronology is compared with the corresponding interval based on the SIOC19 ages. Error bars represent the 2σ age uncertainties on the interval. For the GICC05 chronology, this was calculated as the change in the accumulated layer-counting uncertainty between events (fig. S1); errors are not shown for events within the GICC05modelext section because they are not quantified (32). For the speleothems, the error bar is the uncertainty of the consecutive SIOC19 age estimates in quadrature. The timing between interstadial onsets is shown for those interstadials demonstrated to be synchronous in the speleothems, including estimates based on data from only one region.